J. Fluid Mech. (1991), *vol.* 230, *pp.* 541–582
Printed in Great Britain

Nonlinear oscillations of liquid shells in zero gravity

By N. A. PELEKASIS[1], J. A. TSAMOPOULOS[1]† AND G. D. MANOLIS[2]

[1] Department of Chemical Engineering,
[2] Department of Civil Engineering,
State University of New York at Buffalo, Buffalo, NY 14260, USA

(Received 7 August 1990)

It has been shown experimentally (Lee *et al.* 1982) that water drops with injected air bubbles inside them may be forced dynamically to assume the spherosymmetric shape. Linear analysis is unable to predict a centring mechanism, but provides two distinct modes of oscillation. Weakly nonlinear theory (Tsamopoulos & Brown 1987) indicates that centring of the bubble inside the drop occurs when the two interfaces move out of phase. A hybrid boundary element–finite element schemes is used here to study the complete effect of nonlinearity on the dynamics of the motion. The gas inside the liquid shell may be considered either incompressible or compressible by using a polytropic relation. In both cases, the present calculations show that besides the fast oscillation of the shell due to an initial disturbance, a slow oscillatory motion of the centres of the bubble and the drop is induced around the concentric configuration. This occurs in both modes of oscillation and is a direct result of Bernoulli's law. Furthermore, when this slow oscillation is damped by viscous forces, it is anticipated that it will lead to a spherosymmetric shape.

1. Introduction

In general, compound drops are composed of a fluid core enclosed by a shell made of a second fluid and are immersed in a fluid medium. Both pairs of fluids in contact are considered immiscible. Compound drops have received considerable attention in recent years owing to a variety of applications (Johnson & Sadhal 1985). The most notable application is in manufacturing hollow spherosymmetric shells of metal or glass used in Inertial Confinement Fusion (ICF) as targets (Lee *et al.* 1982; Kendall 1986; Hendricks 1982). Their preparation involves dynamic centring of a bubble inside a liquid drop and subsequent solidification of the system. In another application, hollow shells are used as fillers to produce composite systems of high strength and low weight. The feasibility of the above applications is determined by the concentricity of the shells, which is required for a successful implosion-reaction in ICF and enhances the compactness of the composite material.

Hollow liquid shells are produced by the capillary breakup of an annular liquid jet (Kendall 1986). There is experimental evidence to suggest that compound drops and liquid shells tend to become concentric and resist breakup while undergoing shape oscillations (Lee *et al.* 1982). Shape oscillations may easily be induced while the shells are levitated acoustically. In what follows, the volume inside the inner and outer

† Author to whom correspondence should be addressed.

gas–fluid interfaces will be referred to as bubble and drop, respectively. The region between the two interfaces will be called the liquid shell.

In an effort to predict the aforementioned behaviour, it is assumed that the shell is initially axisymmetric in shape and that only axisymmetric disturbances are allowed. The effect of gravity may be neglected on the grounds that the gravitational Bond number ($\tilde{R}_2^2 g\rho/\sigma$) is small. The liquid shell is assumed to be incompressible, whereas the gas bubble may be either incompressible or compressible. In both cases the pressure in the bubble is uniform, but in the latter case it is allowed to vary with volume changes according to a polytropic law.

Linear analysis in both the high and low Reynolds-number limits has been carried out by Saffren, Elleman & Rhim (1982) and Patzer & Homsy (1975), respectively. Both studies consider axisymmetric disturbances in the form of spherical harmonics of initially concentric configurations. Two modes of oscillation are identified for the shell. In the first one (the so-called bubble mode) both interfaces are moving in phase, while in the second one (the so-called sloshing mode) they move out of phase. The motion is characterized by distinct linear frequencies and decay rates (for viscous fluids). Both studies predict a zero eigenvalue for the mode that represents a translation of the bubble with respect to the drop.

The inability of either viscous or inviscid linear theory to explain experimental observations indicates that nonlinear effects, most notably inertia, should be included in a successful prediction of the centring mechanism. Tsamopoulos & Brown (1987) carried out a weakly nonlinear analysis for the oscillations of an inviscid liquid shell. They predicted that the frequencies of shape oscillations decrease proportionately to ϵ^2 and that centring will occur in a slow timescale ($O(\epsilon^{-2})$, where ϵ is the amplitude of the motion) only when the sloshing mode is excited. More recently, Lee & Wang (1988) considered the limiting case of shell thickness small compared to either of the radii. Their inviscid analysis revealed a slow oscillation of the bubble around the centre of mass of the shell for both the bubble and the sloshing mode. Introduction of weak viscous effects in their model resulted in centring of the bubble inside the drop, which occurred faster for larger initial deformations.

In the present study the exact inviscid and irrotational equations for a liquid shell are solved numerically. The inviscid assumption simplifies the treatment and is appropriate since $Re \gg 1$ and both interfaces are between a gas and a liquid (Lamb 1932). In fact, with water as the liquid in the shell at 20 °C the Reynolds number based on the outer shell radius, $\tilde{R}_2 = 1$ cm, is 866; whereas it decreases to 274 if it is based on the shell thickness, $\tilde{R}_2 - \tilde{R}_1 = 0.1$ cm. In the first case, the boundary-layer thickness, which scales with $Re^{-\frac{1}{2}}$, is much smaller than the characteristic lengthscale (0.03 cm $\ll$ 1 cm); whereas it becomes comparable to it in the second case (0.06 cm $<$ 0.1 cm). The governing equations along with the relevant physical quantities are given in §2. It is a well-known result of potential theory that solutions to Laplace's equation can be found by solving a boundary-integral equation. In general, this equation gives the value of the potential anywhere in the domain in terms of boundary quantities (Kellogg 1953). In moving-boundary problems like the one treated here, this integral equation must be solved along with the kinematic and dynamic boundary conditions for the location of the boundary, the potential and the potential flux there at all times. This integral approach has been used quite extensively in the literature since it reduces the dimensionality of the problem by one and, in some cases, can even exactly satisfy certain boundary conditions.

Longuet-Higgins & Cokelet (1976) were among the first to use this approach in their study of progressive Stokes and breaking waves. They used a Lagrangian

formulation for advancing in time the free surface location and the velocity potential, whereas an integral equation of the first kind was solved for the normal component of the velocity at every time step. However, this scheme gave rise to a short-wave instability that was removed by introduction of artificial viscosity. Dold & Peregrine (1984) studied the same problem by using the Cauchy integral theorem for the complex velocity potential as well as its Eulerian time derivatives up to a certain order. This scheme allowed them to integrate in time without smoothing. In their study of forced oscillations of floating solid bodies, Dommermuth & Yue (1987) used Green's theorem to solve for the normal velocity on the surface. In order to avoid concentration of the Lagrangian markers in regions of high curvature, which causes growth of numerical instabilities, they used remeshing at every time step, which is a form of smoothing.

The method of point vortices has been widely used ever since the work of Rosenhead (1931) in numerical studies of layered flows. Such motions are known to be subject to the Kelvin–Helmholtz and Rayleigh–Taylor instabilities. Baker, Meiron & Orszag (1982, 1984) developed a generalized point-vortex method for studying interfacial wave phenomena. They used point vortices or dipole distributions that generate the velocity potential and are related to it through an integral equation of the second kind. This formulation makes possible an iterative solution with potential savings in both storage and computation time. However, growth of high modes still persists and is suppressed only after decreasing the time step and limiting the length of computations. Furthermore, Pullin (1982) introduced surface tension in his study of Rayleigh–Taylor and Kelvin–Helmholtz instabilities with the point-vortex method. He found that this only delayed the appearance of instabilities and that smoothing was eventually needed. Krasny (1986) used the same method coupled with a new filtering technique. Lundgren & Mansour (1988) were the first to use a dipole distribution for studying capillary oscillations and instabilities of liquid drops. They also observed an oscillatory growth of the higher modes brought about by the numerical discretization of the surface, which was more pronounced close to the poles. They used a standard smoothing technique in order to filter them out of the solution.

The nature of these short-wave instabilities is not exactly known. However, Moore (1981) showed that the chaotic motion observed in all numerical simulations of the Kelvin–Helmholtz instability is a discrete equivalent of the ill-posedness of the continuous set of equations. Subsequently, Moore (1982) studied the evolution of Stokes waves using the point-vortex method and concluded that the sawtooth instability is a result of nonlinear interactions and mode resonance which is facilitated by the distortion of the dispersion relation in the discrete model.

In view of the variety of approaches, choosing a particular numerical scheme is not an easy task. Our choice was dictated by the success of previous attempts, our own experience, and the nature of the problem at hand. To begin with, it is anticipated that the two free surfaces of the liquid shell will not fold over before they touch, at which point both the computational scheme and the physical forces present must be modified. This observation, coupled with the frequent reference in the literature (Lundgren & Mansour 1988; Dommermuth & Yue 1987; Moore 1981) to the need for redistributing the Lagrangian markers in order to avoid their time-dependent and uneven distribution and the resulting instability, make the use of an Eulerian formulation quite attractive. In this context, and in order to make the present formulation truly one-dimensional, the boundary conditions are rewritten in terms of quantities that are defined and can be calculated on the boundaries only. The

necessary transformation in terms of the Hamiltonian variables is provided in §3 and its advantages are discussed.

Choosing between an integral equation of the first or second kind is probably the most important decision that has to be made when using an integral formulation. As pointed out by Baker *et al.* (1984) for axisymmetric problems and by Baker & Shelley (1986) for two-dimensional geometries, the double-layer formulation, when applied to multiply-connected domains, leads to a Fredholm equation of the second kind whose homogeneous form admits non-trivial solutions. Consequently, an additional source term has to be included whose strength must be calculated using the adjoint equation as prescribed by Fredholm's alternative. In order to avoid this additional effort and motivated by the reliability of results obtained previously (Dommermuth & Yue 1987; Pelekasis, Tsamopoulos & Manolis 1990), Green's theorem was chosen for the integral formulation. This integral formulation is described in §4.

In §5, certain invariants of the motion are given. They will be used to check the accuracy of the numerical results. In §6, the numerical methodology is discussed. It involves a hybridization and simultaneous solution of the integral equation via boundary-element methods and the kinematic and dynamic conditions via finite-element methods. This combination brings together the flexibility of the now standardized finite-element methodology with the effectiveness of the integral-equation formalism. Use of this numerical approach permits time integration without smoothing even for moderate deformations, as long as the discretization in space is refined enough. Under severe deformations and as time progresses, computations have to be stopped owing to the growth of short waves. This behaviour will be analysed in §6 also. In §7, the linear solution is given in terms of the eigenmodes and is compared with numerical results for small-amplitude deformations. In addition, the effects of the amplitude of the initial disturbance, of the ratio of the bubble to drop radii and of the gas compressibility are presented. Finally, conclusions are drawn in §8.

2. Eulerian formulation

The oscillatory motions of an inviscid, incompressible and axisymmetric liquid shell are studied here. The shell is immersed in and is surrounded by an inertialess gas. The pressure of the outer gas P_2 is constant, whereas the pressure of the gas inside the bubble P_1 is uniform in space but can vary in time. The density of the liquid in the shell is ρ and the surface tension of either gas–liquid interface is σ. The motion of the shell is induced by initially introducing an axisymmetric deformation of both free surfaces as well as by translating the centre of the bubble with respect to the centre of the drop along the line of symmetry. The radii of the motionless and spherosymmetric shell with the same volume are R_1 and R_2 for the bubble and the drop, respectively. The outer radius R_2 is assigned as the characteristic length of the system. It is used to define the dimensionless shape functions $F_1(\theta, t)$ and $F_2(\theta, t)$ that represent the distance of the two interfaces from the centre of mass of the shell, which is also the origin of the coordinate system. A schematic of the shell is given in figure 1, where θ is the meridional angle in spherical coordinates. As in Tsamopoulos & Brown (1983, 1987), the velocity potential $(\sigma R_2/\rho)^{\frac{1}{2}}\Phi(r, \theta, t)$, pressure $(2\sigma/R_2)P(r, \theta, t)$ and time $(\rho R_2^3/\sigma)^{\frac{1}{2}}t$ are defined in terms of their dimensionless counterparts. Then the equations and boundary conditions governing the motion are

$$\nabla^2\Phi = 0, \quad F_1(\theta, t) \leqslant r \leqslant F_2(\theta, t), \quad 0 \leqslant \theta \leqslant \pi, \tag{2.1}$$

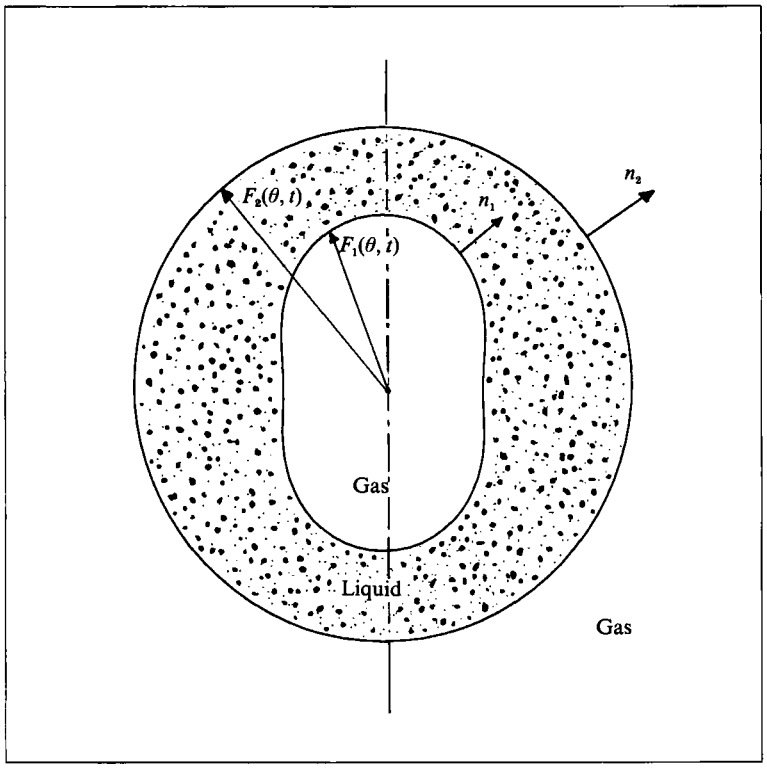

FIGURE 1. Schematic of coordinate system and surface representation used for the description of a liquid shell.

$$\frac{\partial F_1}{\partial \theta} = \frac{\partial F_2}{\partial \theta} = 0, \quad \theta = 0, \pi, \tag{2.2a}$$

$$\frac{\partial \Phi}{\partial \theta} = 0, \quad \theta = 0, \pi, \quad F_1(\theta, t) \leqslant r \leqslant F_2(\theta, t), \tag{2.2b}$$

$$2P + \frac{\partial \Phi}{\partial t} + \tfrac{1}{2}|\nabla \Phi|^2 = 0, \quad F_1(\theta, t) \leqslant r \leqslant F_2(\theta, t), \quad 0 \leqslant \theta \leqslant \pi, \tag{2.3}$$

$$\frac{\partial F_i}{\partial t} = \frac{\partial \Phi}{\partial r} - \frac{1}{r^2}\frac{\partial \Phi}{\partial \theta}\frac{\partial F_i}{\partial \theta}, \quad r = F_i(\theta, t), \quad 0 \leqslant \theta \leqslant \pi, \quad i = 1, 2, \tag{2.4}$$

$$2P_i - 2P = \mp 2\mathscr{H}_i = \pm \nabla_s \cdot \boldsymbol{n}_i, \quad r = F_i(\theta, t), \quad 0 \leqslant \theta \leqslant \pi, \quad i = 1, 2, \tag{2.5}$$

$$V_1 = \frac{2\pi}{3}\int_0^\pi F_1^3(\theta, t)\sin\theta \, \mathrm{d}\theta = \frac{4\pi R^3}{3}, \tag{2.6a}$$

$$V_2 = \frac{2\pi}{3}\int_0^\pi F_2^3(\theta, t)\sin\theta \, \mathrm{d}\theta = \frac{4\pi}{3}, \tag{2.6b}$$

$$P_1(t=0)(2R^3)^\gamma = P_1(t)\left[\int_0^\pi F_1^3(\theta, t)\sin\theta \, \mathrm{d}\theta\right]^\gamma. \tag{2.6c}$$

Laplace's equation (2.1) governs the irrotational flow inside the shell, which remains axisymmetric due to (2.2). In the absence of viscous effects, Bernoulli's equation

describes the pressure variation inside the shell, (2.3). Equations (2.4) are the kinematic conditions that govern the time evolution of either interface. The dynamic boundary conditions, (2.5), describe the balance between the capillary force and the pressure drop across the interface. In these equations, $\mathscr{H}_i$ denote the mean curvatures, $\boldsymbol{n}_i$ the outwards-pointing normals of either interface and ∇_s is the surface gradient. For convenience, the inwards-pointing normal to the bubble that will be used later is defined as $\boldsymbol{n}_1' = -\boldsymbol{n}_1$. The unit normals and mean curvatures can be expressed in terms of the shape functions of each interface as

$$\boldsymbol{n}_i = (F_i \boldsymbol{e}_r - F_{i,\theta} \boldsymbol{e}_\theta)(F_i^2 + F_{i,\theta}^2)^{-\frac{1}{2}} \equiv n_{i,r} \boldsymbol{e}_r + n_{i,\theta} \boldsymbol{e}_\theta, \tag{2.7}$$

$$-2\mathscr{H}_i = \left\{ -\frac{F_{i,\theta\theta}}{F_i} - \cot\theta \frac{F_{i,\theta}}{F_i}\left[1 + \left(\frac{F_{i,\theta}}{F_i}\right)^2\right] + 2 + 3\left(\frac{F_{i,\theta}}{F_i}\right)^2 \right\} \left\{ F_1 \left[1 + \left(\frac{F_{i,\theta}}{F}\right)^2\right]^{\frac{3}{2}} \right\}^{-1}. \tag{2.8}$$

Also, subscript θ denotes partial differentiation with respect to that coordinate. When the bubble is considered to be incompressible, its volume remains constant according to (2.6a), where $R \equiv R_1/R_2$. This equation is used to calculate the pressure inside the bubble. Equation (2.6b) sets the volume of the drop as constant, thus assuring that the volume of the shell, $V_2 - V_1$, is conserved. This is done in order to exclude the zeroth mode from the numerical solution since it may grow exponentially (see Tsamopoulos & Brown 1987). For further discussion see §6. Alternatively, the pressure inside the gas bubble may be allowed to change, assuming that it undergoes an adiabatic or polytropic variation. Then, (2.6c) must be used instead of (2.6a) and (2.6b) and γ may be taken to be between 1 and 1.4.

As mentioned earlier, the shell is perturbed to an axisymmetric shape, but no initial velocity is imparted to it, i.e.

$$\partial F_i / \partial t(\theta, t = 0) = 0, \quad i = 1, 2, \tag{2.9}$$

so that the initial velocity is zero and the motion irrotational, and remains so in the absence of viscosity. Following earlier work (Tsamopoulos & Brown 1983, 1987), this initial disturbance is selected such that the shape of the shell is given by the normal mode solution and is correct to $O(\epsilon^2)$. The perturbation to the outer surface is

$$F_2(\theta, t = 0) = 1 + \epsilon[R^4 P_1(\theta) + P_2(\theta)] + \epsilon^2(-\tfrac{1}{5} - \tfrac{1}{3}R^8) + O(\epsilon^3), \tag{2.10a}$$

where $P_n(\theta)$ is the Legendre polynomial of the nth degree. The initial deformation of the inner surface is

$$F_1(\theta, t = 0) = R\{1 + \epsilon[P_1(\theta) + BP_2(\theta)] + \epsilon^2[-\tfrac{1}{3} - \tfrac{1}{5}B^2 + \tfrac{6}{5}(1 - B)P_1(\theta)]\} + O(\epsilon^3), \tag{2.10b}$$

where B is a constant given by Tsamopoulos & Brown (1987). The first Legendre polynomial is responsible for the initial displacement of the centres of mass of the bubble and drop. Clearly, the centre of mass of the shell remains at zero, since no external force is applied on it. The second Legendre polynomial distorts the shape of the shell in one of the two normal modes, to a magnitude measured by ϵ and in such a way that the two interfaces do not intersect initially.

The disturbances described in (2.10) are such that the volumes of the drop and the bubble are conserved (up to second order in ϵ) and correspond to volumes of spheres of radii 1.0 and R, respectively. Similarly, the centre of mass of the shell is set to zero, again up to second order in ϵ. Almost all of the results to be presented later have been obtained with these initial conditions. In an effort to study the effect of an initial

displacement of the centre of mass of the bubble on the motion, we also used the following initial conditions:

$$F_2(\theta, t=0) = 1+\epsilon P_2(\theta)-\tfrac{1}{5}\epsilon^2, \tag{2.11a}$$

$$F_1(\theta, t=0) = R+\Delta P_1(\theta)+\epsilon P_2(\theta)B-\epsilon^2 R[(B/R)^2+\tfrac{1}{3}]. \tag{2.11b}$$

The above conditions conserve volume up to second order in ϵ, but set the centre of mass of the drop to zero while displacing the centre of mass of the bubble away from zero by an amount that depends on the value of the independent parameter Δ. As a result, the centre of mass of the shell is displaced from the origin of the coordinate system to a different location and remains there.

As a third alternative for initial condition both interfaces are taken to be spherical and the centre of the inner one is displaced upwards by Δ from the centre of the outer one:

$$F_2(\theta, t=0) = 1, \tag{2.12a}$$

$$F_1(\theta, t=0) = \Delta\cos\theta+(R^2-\Delta^2\sin^2\theta)^{\frac{1}{2}}. \tag{2.12b}$$

No shape oscillations can arise from this originally static configuration unless there is a variation in the outer gas pressure.

3. Formulation in terms of the canonical variables

The goal is to end up with a representation of the motion in terms of surface quantities. In particular, the location of the boundary and the value of the potential there have been shown by Miles (1977) to be the canonical variables of the Hamiltonian for water wave problems. These two are naturally the most suitable variables for a description of the motion. To this end, two new variables are introduced as

$$\psi_i(\theta, t) = \Phi(r = F_i(\theta, t), \theta, t), \quad i = 1, 2. \tag{3.1}$$

They are the values of the potential at each interface and obey the same initial and symmetry conditions imposed on Φ earlier. In what follows, the governing equations will be restated in terms of ψ_i, F_i and $\partial\Phi/\partial n_i$. The chain rule is applied first in order to evaluate the derivatives of ψ_i as

$$\left.\frac{\partial\psi_i}{\partial\theta}\right|_t = \left.\frac{\partial\Phi}{\partial\theta}\right|_{t, r, r=F_i(\theta,t)} + \left.\frac{\partial\Phi}{\partial r}\right|_{t, \theta, r=F_i(\theta,t)} \left.\frac{\partial F_i}{\partial\theta}\right|_t, \quad i = 1, 2, \tag{3.2}$$

$$\left.\frac{\partial\psi_i}{\partial t}\right|_\theta = \left.\frac{\partial\Phi}{\partial t}\right|_{\theta, r, r=F_i(\theta,t)} + \left.\frac{\partial\Phi}{\partial r}\right|_{\theta, t, r=F_i(\theta,t)} \left.\frac{\partial F_i}{\partial t}\right|_\theta, \quad i = 1, 2. \tag{3.3}$$

Using the definition of the gradient operator and the normal unit vectors to either interface, the derivative $\partial\Phi/\partial r|_{t,\theta,r=F_i}$ is expressed in terms of normal and meridional derivatives of the potential as

$$\left.\frac{\partial\Phi}{\partial r}\right|_{t, \theta, r=F_i(\theta,t)} = \frac{\partial\Phi}{\partial n_i} F_i(F_i^2+F_{i,\theta}^2)^{-\frac{1}{2}} + \frac{\partial\psi_i}{\partial\theta}\frac{\partial F_i}{\partial\theta}(F_i^2+F_{i,\theta}^2)^{-1}, \quad i = 1, 2. \tag{3.4}$$

Substituting (3.2) and (3.4) into the kinematic condition results in

$$\frac{\partial F_i}{\partial t} = \frac{\partial\Phi}{\partial n_i}\frac{1}{F_i}(F_i^2+F_{i,\theta}^2)^{\frac{1}{2}}, \quad i = 1, 2. \tag{3.5}$$

The same result can be obtained by combining (2.4) written for $f(\theta,t) = r - F(\theta,t) = 0$ with the definition of $\boldsymbol{n} = \nabla f/|\nabla f|$, and with $\partial\phi/\partial n = \boldsymbol{n}\cdot\nabla\Phi$. However, the derivation above is preferred because it can be used for both the kinematic and the dynamic condition. Combining (3.2)–(3.4) with Bernoulli's equation and the normal force balances at each interface results in

$$\frac{\partial\phi_i}{\partial t} + 2P_i \pm 2\mathscr{H}_i - \frac{1}{2}\left(\frac{\partial\phi}{\partial n_i}\right)^2 + \frac{1}{2}\left(\frac{\partial\psi_i}{\partial\theta}\right)^2 (F_i^2 + F_{i,\theta}^2)^{-1} \pm \frac{\partial\phi}{\partial n_i}\frac{F_{i,\theta}}{F_i}\frac{\partial\psi_i}{\partial\theta}(F_i^2 + F_{i,\theta}^2)^{-\frac{1}{2}} = 0, \quad i = 1,2. \tag{3.6}$$

The final relationship between the normal derivatives of the potential and its values at the two interfaces will be provided by the Laplacian (equation (2.1)). This can be written schematically as follows:

$$L\left(\psi_1, \frac{\partial\Phi}{\partial n_1}, \psi_2, \frac{\partial\phi}{\partial n_2}\right) = 0, \quad r = F_i(\theta,t), \quad 0 \leqslant \theta \leqslant \pi, \quad i = 1,2, \tag{3.7}$$

and is dealt with in §4.

Thus, (2.1)–(2.5) have been substituted by (3.5)–(3.7). The fact that F and ψ are the canonical variables of the Hamiltonian was also shown earlier by Zakharov (1968). Both he & Miles (1977) used a spectral representation of F and ψ in order to study stability of periodic water waves. The above formulation has an important advantage when carrying out numerical calculations. The radial coordinate, r, has been eliminated and the partial derivatives are taken with constant θ or t, as opposed to the original formulation where r had to be kept constant as well. Clearly, if all relationships are to be written on the interfaces, r is bound to change both with time and with the meridional angle. This makes the numerical differentiation holding r constant rather ambiguous. In contrast, the current formulation makes the one-dimensional character of the problem apparent and the numerical implementation straightforward.

4. Integral formulation

In order to obtain a relationship between the potential and its normal derivative on the two interfaces, Green's third identity is applied as follows:

$$\alpha\Phi(\boldsymbol{x}',t) + \int_A \Phi(\boldsymbol{x},t)\frac{\partial\hat{G}}{\partial n}(\boldsymbol{x},\boldsymbol{x}')\,\mathrm{d}A(\boldsymbol{x},t) = \int_A \frac{\partial\Phi}{\partial n}(\boldsymbol{x},t)\,\hat{G}(\boldsymbol{x},\boldsymbol{x}')\,\mathrm{d}A(\boldsymbol{x},t), \tag{4.1}$$

where A comprises both shell interfaces and $\boldsymbol{n}$ is the outwards-pointing normal for the domain of the shell, i.e. it is either $\boldsymbol{n}_2$ or $\boldsymbol{n}_1'$. Furthermore, $\hat{G}$ is the three-dimensional free-space singular solution of the Laplacian subject to a point force at the source point $\boldsymbol{x}(r,\theta,\phi)$ and $\partial\hat{G}/\partial n$ is its normal derivative. In spherical coordinates, $\hat{G}(\boldsymbol{x},\boldsymbol{x}')$ is given by

$$\hat{G}(\boldsymbol{x},\boldsymbol{x}') = \frac{1}{4\pi}[(r\sin\theta\cos\phi - r'\sin\theta'\cos\phi')^2 + (r\sin\theta\sin\phi - r'\sin\theta'\sin\phi')^2 + (r\cos\theta - r'\cos\theta')^2]^{-\frac{1}{2}}. \tag{4.2}$$

If the field point, $\boldsymbol{x}'(r',\theta',\phi')$, is in the exterior (interior) of the shell, the jump-term coefficient α is equal to 0 (1). If it lies on one of the two surfaces, it will coincide with

one of the source points $\boldsymbol{x}(r,\theta,\phi)$ and then α is given by the angle subtended by the planes tangent to the surface at that point. For a smooth surface, α is equal to 0.5. In the latter case, the integral on the left-hand side of (4.1) is to be understood in the Cauchy principal value sense. In order to extract the singularity from the integral, the value of the potential at the field point is added and subtracted:

$$\tfrac{1}{2}\Phi(\boldsymbol{x}',t)+\int[\Phi(\boldsymbol{x},t)-\Phi(\boldsymbol{x}',t)]\frac{\partial\hat{G}}{\partial n}(\boldsymbol{x},\boldsymbol{x}')\,\mathrm{d}A(\boldsymbol{x},t)$$

$$+\int\Phi(\boldsymbol{x}',t)\frac{\partial\hat{G}}{\partial n}(\boldsymbol{x},\boldsymbol{x}')\,\mathrm{d}A(\boldsymbol{x},t)=\int\frac{\partial\phi}{\partial n}(\boldsymbol{x},t)\,\hat{G}(\boldsymbol{x},\boldsymbol{x}')\,\mathrm{d}A(\boldsymbol{x},t). \quad (4.3)$$

In this form, the integrand in the first integral on the left-hand side of (4.3) is regular since $\Phi(\boldsymbol{x},t)-\Phi(\boldsymbol{x}',t)$ tends to be zero as the field point approaches the source point at the same rate with which $\partial\hat{G}/\partial n$ becomes singular in this neighbourhood. In the second integral, $\Phi(\boldsymbol{x}',t)$ is constant as far as the integration in $\boldsymbol{x}(r,\theta,\phi)$ is concerned and can be taken outside the integral sign, thus leaving a well-known Cauchy principal value integral:

$$\Phi(\boldsymbol{x}',t)\int_A\frac{\partial\hat{G}}{\partial n}(\boldsymbol{x},\boldsymbol{x}')\,\mathrm{d}A(\boldsymbol{x},t)=-\tfrac{1}{2}\Phi(\boldsymbol{x},t). \quad (4.4)$$

Inserting this expression in (4.3) yields

$$\int_A[\Phi(\boldsymbol{x},t)-\Phi(\boldsymbol{x}',t)]\frac{\partial\hat{G}}{\partial n}(\boldsymbol{x},\boldsymbol{x}')\,\mathrm{d}A(\boldsymbol{x},t)=\int_A\frac{\partial\Phi}{\partial n}(\boldsymbol{x},t)\,\hat{G}(\boldsymbol{x},\boldsymbol{x}')\,\mathrm{d}A(\boldsymbol{x},t). \quad (4.5)$$

For axisymmetric problems ϕ' can be set equal to zero in $\hat{G}$ and $\partial\hat{G}/\partial n$. Then, the integrations indicated in (4.5) can be carried out with respect to ϕ, resulting in

$$\sum_{i=1}^{2}\int_0^{\pi}[\psi_i(\theta,t)-\psi_1(\theta',t)](-1)^i\frac{\partial G}{\partial n_i}(F_i,F_1',\theta,\theta')\,F_i(F_i^2+F_{i,\theta}^2)^{\frac{1}{2}}\sin\theta\,\mathrm{d}\theta$$

$$=\sum_{i=1}^{2}\int_0^{\pi}(-1)^i\frac{\partial\Phi}{\partial n_i}(\theta,t)\,G(F_i,F_i',\theta,\theta')\,F_i(F_i^2+F_{i,\theta}^2)^{\frac{1}{2}}\sin\theta\,\mathrm{d}\theta \quad (4.6)$$

when the field point is taken to the inner surface. When the field point is taken to the outer surface, the resulting expression is similar to (4.6) except that the subscript 1 must be substituted by 2.

In addition,

$$G=\int_0^{2\pi}\hat{G}\,\mathrm{d}\phi,\quad \frac{\partial G}{\partial n}=\int_0^{2\pi}\frac{\partial\hat{G}}{\partial n}\mathrm{d}\phi. \quad (4.7)$$

These last two integrals can be written in terms of elliptic integrals of the first and second kind as will be explained in §6. Equation (4.6) constitutes a Fredholm integral equation of the first kind when solved for the flux on the boundaries. However, in the present scheme all unknowns are calculated simultaneously (for reasons presented in §6) and this does not allow for this classification of the integral equation as first or second kind.

5. Invariants of the motion

A very important test on the accuracy of the numerical results consists of

monitoring the values of certain quantities that are known to be invariant in time. Such a quantity is the total mass outflux across each one of the interfaces:

$$I_i = \int_{A_i} \frac{\partial \Phi}{\partial n_i} \mathrm{d}A_i = 2\pi \int_0^{\pi} \frac{\partial \Phi}{\partial n_i} F_i (F_i^2 + F_{i,\theta}^2)^{\frac{1}{2}} \sin\theta \, \mathrm{d}\theta, \quad i = 1, 2. \tag{5.1}$$

I_i have to be zero for an incompressible bubble. Equations (5.1) can be obtained by combining the volume conservation equations for the drop and bubble with the kinematic boundary conditions. If the bubble is considered to be compressible, then the mass flux across each individual surface may vary but the difference $I_2 - I_1$ has to be zero since it represents the total mass outflux across the shell surfaces. This fact can be shown by applying Gauss' theorem on the Laplacian. Another way of assuring overall mass conservation of the shell is by requiring its volume to remain constant:

$$\int_0^{\pi} (F_2^3 - F_1^3) \sin\theta \, \mathrm{d}\theta = 2(1 - R^3). \tag{5.2}$$

This expression can also be derived by integrating the equation of continuity over the volume of the shell and applying the kinematic boundary conditions.

In the absence of any external forces, the centre of mass of the shell has to remain stationary, since no initial velocity was imparted to it at $t = 0$. This is stated as follows:

$$Z_{\mathrm{sh}} \equiv \left[\frac{3}{4} \int_0^{\pi} (F_2^4 - F_1^4) \cos\theta \sin\theta \, \mathrm{d}\theta\right] \left[\int_0^{\pi} (F_2^3 - F_1^3) \sin\theta \, \mathrm{d}\theta\right]^{-1} = 0. \tag{5.3}$$

Equation (5.3) defines the component of the displacement, Z_{sh}, of the centre of mass of the shell along the axis of symmetry. The other two components are identically zero owing to the axial symmetry in the present problem. Clearly, the centre of mass of either the bubble or the drop may vary in time. Their respective expressions are

$$Z_i \equiv \left[\frac{3}{4} \int_0^{\pi} F_i^4 \cos\theta \sin\theta \, \mathrm{d}\theta\right] \left[\int_0^{\pi} F_i^3 \sin\theta \, \mathrm{d}\theta\right]^{-1}, \quad i = 1, 2. \tag{5.4}$$

An alternative analytical way to arrive at (5.3) and (5.4) is to combine the volume integrals of Euler's equation of motion and of the product of Laplace's equation with the z-coordinate.

Since viscosity is assumed to be negligible, the motion of the liquid shell is conservative and its total energy E (kinetic and surface) is invariant. Thus:

$$E = E_{\mathrm{k}} + E_{\mathrm{s}} \equiv \frac{1}{2} \int |\nabla \Phi|^2 \, \mathrm{d}V + \int \mathrm{d}A. \tag{5.5}$$

Applying Gauss' theorem on the volume integral and splitting the surface integrals into each surface results in

$$E = \pi \sum_{i=1}^{2} (-1)^i \int_0^{\pi} \Phi_i \frac{\partial \phi}{\partial n_i} F_i (F_i^2 + F_{i,\theta}^2)^{\frac{1}{2}} \sin\theta \, \mathrm{d}\theta + 2\pi \sum_{i=1}^{2} \int_0^{\pi} F_i (F_i^2 + F_{i,\theta}^2)^{\frac{1}{2}} \sin\theta \, \mathrm{d}\theta. \tag{5.6}$$

The invariance of (5.6) can also be shown by using

$$\int \frac{\partial \Phi}{\partial t} \nabla^2 \Phi \, \mathrm{d}V = 0, \tag{5.7}$$

and then proceeding with integration by parts and employing the kinematic and dynamic boundary conditions.

When the bubble is considered to be compressible, the total energy of the shell is still conserved. However, besides the kinetic and surface energies one has to include the energy that is exchanged with the surrounding gas medium due to volume variations, i.e.

$$E = E_k + E_s + 2P_2 V_2 + \frac{2P_1 V_1}{\gamma - 1}. \tag{5.8}$$

In the above, V_1 and V_2 denote the instantaneous volume of the bubble and the drop, respectively.

6. Numerical inplementation

In its final form, the problem consists of (2.2), (2.9)–(2.12), (3.5), (3.6), and (4.6). In addition, (2.6*a*) and (2.6*b*) are used when the bubble is incompressible, whereas (2.6*c*) is used when compressibility effects are taken into consideration. Equation (2.6*b*) is not linearly independent and is used instead of one of the discretized equations corresponding to the kinematic boundary condition on the outer interface. The unknowns of the problem are the location of the boundary, the potential and the flux on each of the interfaces along with the pressure inside the bubble. These are calculated by the kinematic and dynamic boundary conditions, the Laplacian and the conservation equation of the bubble volume, respectively. The ratio of the radii, R, the initial displacement of the centres of mass and the amplitude of the initial disturbance are the problem parameters. When compressibility effects are considered a pressure datum is also needed.

In order to ensure linear stability of the numerical scheme and high accuracy, the time-implicit trapezoidal rule was chosen. An additional advantage of an implicit scheme over an explicit one is in updating the pressure. For a compressible bubble this is achieved through the polytropic or adiabatic relation. When the bubble is incompressible, however, the volume conservation equation does not involve the internal pressure. This makes the task of updating the pressure or the surface potential rather ambiguous. On the other hand, use of an implicit scheme allows for solution of all the unknowns simultaneously. As a result, the unknown pressure may be associated with the volume conservation equation even though it does not appear explicitly in it.

The trapezoidal rule is second-order accurate and requires iterative solution of a nonlinear set of equations and simultaneous inversion of the total problem matrix. The initial guess at every time step for the iterative solution of the coupled oscillations is provided by the second-order Adams–Bashforth predictor. Also, equidistant time steps are used. The efficiency of the trapezoidal rule compared with that of an explicit scheme is eventually decided by the interplay of numerical stability and accuracy. The fourth-order Runge–Kutta algorithm was also used for the case of a compressible bubble and with the same time step and spatial discretization as that used for the trapezoidal rule. It was found that the Runge–Kutta algorithm was roughly 1.5 times faster, as well as more accurate since it is a higher-order scheme. For reasons of consistency, however, it was decided to use the trapezoidal rule throughout the present study.

As previously shown, the problem has been successfully reduced to one spatial dimension, namely the meridional angle θ. An equidistant mesh in θ is employed

since formation of regions of excessively high curvature is not anticipated. Moreover, an equidistant spatial discretization has been shown to smooth out short-wave instabilities (Dommermuth & Yue 1987; Moore 1981; Lungren & Mansour 1988). Equations (3.5) and (3.6) are discretized using the finite-element procedure. The product of the basis functions times $\sin\theta$ is used as the weighting function. Integration by parts eliminates second-order derivatives from the mean curvature term. The boundary conditions (2.2) are applied in order to evaluate the terms integrated out from the weak finite-element formulation.

Cubic B-splines (de Boor 1978), which are actually cubic polynomials, are used as basis functions in representing $F_i, \psi_i, \partial\Phi/\partial n_i, i = 1, 2$. For example,

$$F_1(\theta, t) = \sum_{j=0}^{N+1} a_j(t) B_j(\theta), \tag{6.1a}$$

$$\psi_1(\theta, t) = \sum_{j=0}^{N+1} b_j(t) B_j(\theta), \tag{6.1b}$$

$$\frac{\partial\Phi}{\partial n_1}(\theta, t) = \sum_{j=0}^{N+1} d_j(t) B_j(\theta), \tag{6.1c}$$

where B_j are the B-splines, a_j, b_j, d_j are the unknown coefficients for the inner surface, potential and flux respectively and N is the number of nodal points in $0 \leqslant \theta \leqslant \pi$. The B-splines were preferred because they guarantee continuity of the function and its first and second derivatives which (hopefully) minimizes the possibility of short-wave instability. Furthermore, the B-splines interpolate a smooth function and its first derivative to $O(h^4)$ and $O(h^3)$ respectively, where h is the maximum element length. Four Gauss points are used for the evaluation of integrals over an element. This ensures that the numerical error is controlled by the interpolation of the derivative of the unknown function. Further details on the implementation of B-splines are given in Pelekasis *et al.* (1990). In this fashion, the kinematic and dynamic boundary conditions may be written schematically as

$$\boldsymbol{M}\frac{\mathrm{d}\boldsymbol{a}}{\mathrm{d}t} = \boldsymbol{F}_1, \quad \boldsymbol{M}\frac{\mathrm{d}\boldsymbol{b}}{\mathrm{d}t} = \boldsymbol{F}_2, \tag{6.2}$$

where $\boldsymbol{M}$ is the common mass matrix and $\boldsymbol{F}_1, \boldsymbol{F}_2$ are the forcing vectors, respectively. The time integration scheme may now be readily applied. The volume conservation equations and the polytropic relation are already in integral form and need not be discussed further.

Discretization of the integral equation (4.6) is done in a fashion similar to that of the boundary conditions. The domain is represented by boundary elements and a system of $2N$ equations is obtained by allowing the field point to coincide with each of the nodes. The two kernels appearing in this equation are given by

$$G = \frac{K(m)}{\pi(a+b)^{\frac{1}{2}}}, \tag{6.3}$$

$$\frac{\partial G}{\partial n} = \left\{\frac{n_r}{2F}\left[\frac{F'^2 - F^2}{a-b}E(m) - K(m)\right] + n_\theta F'\left[\frac{4\cos\theta\sin\theta'}{a+b}\frac{\mathrm{d}K}{\mathrm{d}m} - \frac{\sin(\theta+\theta')}{a-b}\right]\right\}[\pi(a+b)^{\frac{1}{2}}]^{-1}, \tag{6.4}$$

where

$$a = F^2 + F'^2 - 2FF'\cos\theta\cos\theta', \tag{6.5}$$

$$b = 2FF' \sin\theta \sin\theta', \tag{6.6}$$

$$m = 2b/(a+b), \tag{6.7}$$

and (r', θ') is the field point, (r, θ) is the source point, and (n_r, n_θ) are the radial and meridional components of the outward-pointing unit normal at the source point. Finally, $K(m)$ and $E(m)$ are elliptic integrals of the first and second kind, respectively, given by Abramowitz & Stegun (1972). When the field point does not fall on the element where integrations are being carried out, the integrands in (4.6) are regular. Normal Gaussian quadrature is used with a variable number of Gauss points that depends on the distance between the field and the source points (Lachat & Watson 1976). When the field point coincides with one of the source points the G kernel becomes logarithmically singular, while the $\partial G/\partial n$ kernel has an $|\boldsymbol{x}' - \boldsymbol{x}|^{-1}$ singularity. However, as it was pointed out in §4, the $|\boldsymbol{x}' - \boldsymbol{x}|^{-1}$ singularity is being cancelled out by the term $[\psi(\theta, t) - \psi(\theta', t)]$, thus making the integrand regular and allowing for Gaussian quadrature. The integral involving the G kernel has to be treated by means of a special 12-point logarithmic quadrature. For a more detailed discussion on these aspects the reader is referred to Pelekasis *et al.* (1990).

Having carried out the spatial and time integration, a set of $6N+1$ nonlinear algebraic equations are obtained, which are schematically written as

$$\boldsymbol{R}(\boldsymbol{Y}) = \boldsymbol{0}, \tag{6.8}$$

where $\boldsymbol{Y}^{\mathrm{T}} = (\boldsymbol{a}_1^{\mathrm{T}}, \boldsymbol{a}_2^{\mathrm{T}}, \boldsymbol{b}_1^{\mathrm{T}}, \boldsymbol{b}_2^{\mathrm{T}}, \boldsymbol{d}_1^{\mathrm{T}}, \boldsymbol{d}_2^{\mathrm{T}}, P_1)$. This set is solved by Newton's method, which starts with an initial guess $\boldsymbol{Y}^0$ and then calculates successive approximations to the solution as

$$\boldsymbol{Y}^{(k+1)} = \boldsymbol{Y}^{(k)} - \boldsymbol{J}^{-1}\boldsymbol{R}(\boldsymbol{Y}^{(k)}), \quad k = 0, 1, \ldots. \tag{6.9}$$

The Jacobian matrix $\boldsymbol{J} = \partial \boldsymbol{R}/\partial \boldsymbol{Y}$ is analytically calculated and its part that arises from the integral equation is fully populated. A standard IMSL routine (DLFTRG) is used for its factorization. Typically, three to four Newton Iterations are sufficient to reduce the error, defined in terms of the Euclidean norm, $|\boldsymbol{Y}^{(k+1)} - \boldsymbol{Y}^{(k)}|_2$, to less than 10^{-8}.

Since the calculation of the elements of the Jacobian matrix corresponding to the Laplacian involves differentiation of the already singular kernels (G and $\partial G/\partial n$), one might expect that this will give rise to even stronger singularities. However, as explained in Pelekasis *et al.* (1990), this is not true since at the singular point G and $\partial G/\partial n$ will depend on the coefficient Y_i both through F and F'. Furthermore, it may be readily shown that at the singular point the strongly singular part of $\partial G/\partial F$ is cancelled out by the equivalent singular part of $\partial G/\partial F'$. Similarly, the most singular part of $\partial^2 G/\partial n\, \partial F$ is counteracted by the most singular part of $\partial^2 G/\partial n\, \partial F'$ in such a way that they eliminate each other at the singular point. As a result of this, the Jacobian elements will be at most as singular as the residual terms from which they stemmed and consequently can be integrated as shown before.

The numerical scheme described thus far can be used for tracing the motion of the shell, provided that the two interfaces do not touch or fold over. In these cases, their description would not be a single-valued function of the meridional angle. Another important characteristic of the motion of a shell surrounding an incompressible bubble is that the zeroth mode is observed to grow exponentially fast for any value of R. The same situation occurs in the compressible case for a certain range of values of the internal pressure depending on R. Since the zeroth mode corresponds to a uniform inflation of a bubble, imposing the volume conservation for the in-

compressible case and solving for the Laplacian should in principle guarantee conservation of volume for both bubble and drop. However, the discrete equations will contain the zeroth mode due to a small round-off error. This mode will grow as predicted by the linear theory and eventually become the dominant one. In order to rule it out, the volume conservation is explicitly imposed on the drop also. Since this is not a linearly independent equation, it enters the formulation in place of one of the discrete equations corresponding to the kinematic boundary condition on the outer surface.

The accuracy of the method was first tested on the linear problem for which an analytical solution exists (Tsamopoulos & Brown 1987). Upon mesh refinement, the numerical scheme exhibits $O(\Delta t^2)$ and $O(h^3)$ convergence. This is expected since the trapezoidal rule is second-order accurate and the most important error in the spatial discretization is in interpolating derivatives of the boundary shapes. No variation of the linear energy is observed, and the boundary shapes are always calculated more accurately than either the potential or the flux.

The most commonly observed numerical difficulty in free-surface flows is the growth of short-wavelength modes with time. As argued by several investigators (Moore 1982; Lundgren & Mansour 1988) this is a nonlinear instability since it grows faster for larger values of the initial deformation. One has to be careful in recognizing this, since high modes are naturally expected to grow, albeit slowly in time, due to nonlinear coupling. Therefore, as time increases they are expected to become more important. In addition to this physical growth, the numerical instability is channelling energy to the higher modes from the lower ones, thus accelerating their growth. This probably occurs through resonance between the initially excited modes and the higher ones, due to inaccuracies in the numerical dispersion relation (Moore 1982).

In the present formulation, detection and suppression of this numerical error is achieved by refinement of the discretization in both space and time, but without resorting to numerical smoothing. Short-wave instabilities are more apparent when the bubble mode is initially excited. The reason for this is that for the same values of ϵ and R, the relative deformation of the two surfaces is larger in the bubble mode than in the sloshing mode, as shown in figure 4 of Tsamopoulos & Brown (1987) and in Lee & Wang (1988). Under the same conditions, the two surfaces touch each other faster in the sloshing mode since they move out of phase and this occurs before numerical instabilities have a chance to grow significantly. Touching of the two surfaces may be completely avoided for oscillation in the bubble mode and for the same values of ϵ and R.

In an effort to investigate the behaviour of the numerical code with respect to the growth of high modes, the bubble mode was excited with $R = 0.7$. Forty boundary elements per surface were used. The time step was set at $\Delta t = 0.002$, which resulted in roughly 440 steps for one period of this mode as predicted by linear theory. Three different values of the initial disturbance were used, i.e. 0.05, 0.10 and 0.15. For $\epsilon = 0.15$ the computations broke down at $t = 2.268$ in the sense that Newton's iterations failed to converge. It was found that the energy increased just before this failure.

The growth of the higher modes is most clearly seen by plotting the flux through the inner surface, which deteriorates more and earlier than the interface shape and potential do. Figure 2(*c*) shows the significant increase of the P_{40} mode for $\epsilon = 0.15$. In contrast to this, when $\epsilon = 0.05$ or 0.1, integration is carried out for as long as 10 periods of oscillation, as shown in figures 2(*a*) and 2(*b*). There is a noticeable increase of the high modes in the flux for $\epsilon = 0.1$, but this does not affect the calculations

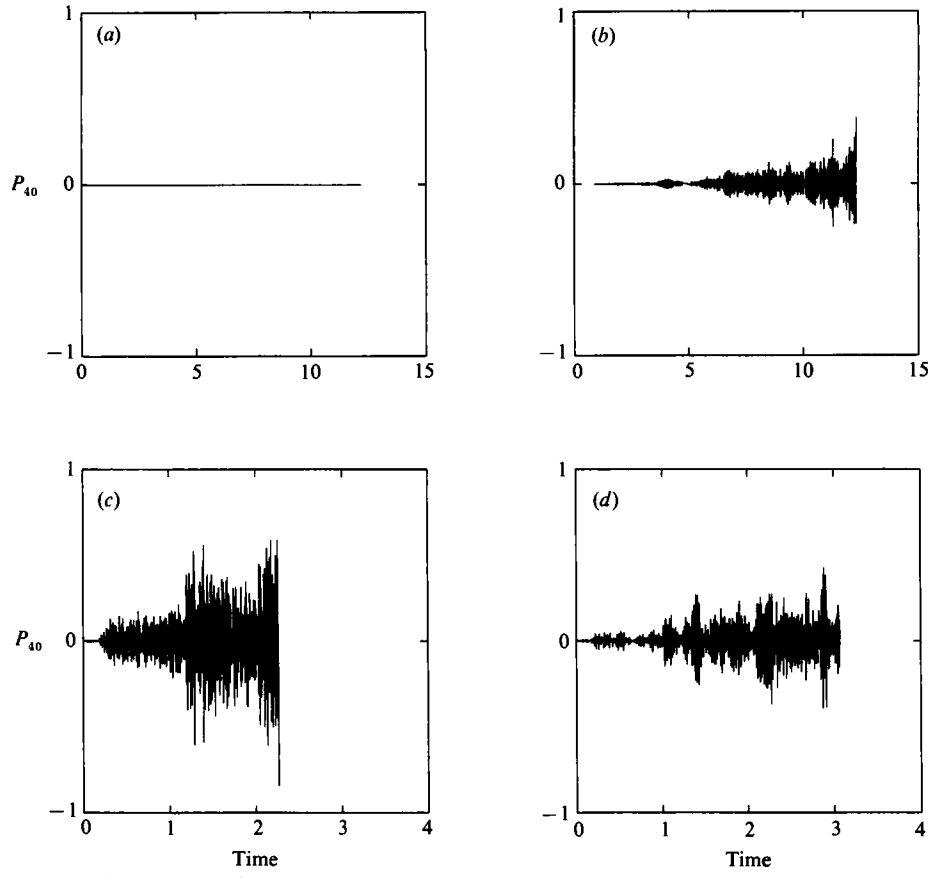

FIGURE 2. Amplitude of 40th mode of the flux through the inner surface for (*a*) $\epsilon = 0.05$ and 40 elements per surface; (*b*) $\epsilon = 0.1$ and 40 elements; (*c*) $\epsilon = 0.15$ and 40 elements and (*d*) $\epsilon = 0.15$ and 60 elements per surface.

significantly. The shape of the shells and the fluxes through each surface for $\epsilon = 0.05$, 0.1 and 0.15 are shown in figures 3(*a*), 4(*a*), 3(*b*), 4(*b*); and 3(*c*), 4(*c*), respectively, just before the computations collapse for the $\epsilon = 0.15$ case. A gradual loss of smoothness is observed.

In order to verify that numerical discretization is responsible for this failure, the calculations were repeated using 60 elements per surface for $\epsilon = 0.15$. Integration failed again, but at a later time, i.e. at $t = 3.066$. When the time step was halved, calculations were carried out further, until $t = 3.688$. At that point, the two surfaces seem to touch each other at the north pole. As can be seen in figure 2(*d*), the oscillations of P_{40} are considerably suppressed when 60 elements are used. Similarly, the energy is not observed to vary as much. At the same time, the P_{60} mode is increasing rapidly before the two surfaces touch, as seen in figure 5. It is quite important to notice that in spite of these observations for the fluxes, the interface shapes are quite smooth, as seen in figures 3(*c*) and 3(*d*). More importantly, however, agreement up to the second significant digit is observed between the shapes shown in figures 3(*c*) and 3(*d*) which were obtained with 40 and 60 elements, respectively, and for $\epsilon = 0.15$. This indicates that 40 elements are sufficient in order to obtain a numerically accurate solution for the shape, even under these adverse conditions.

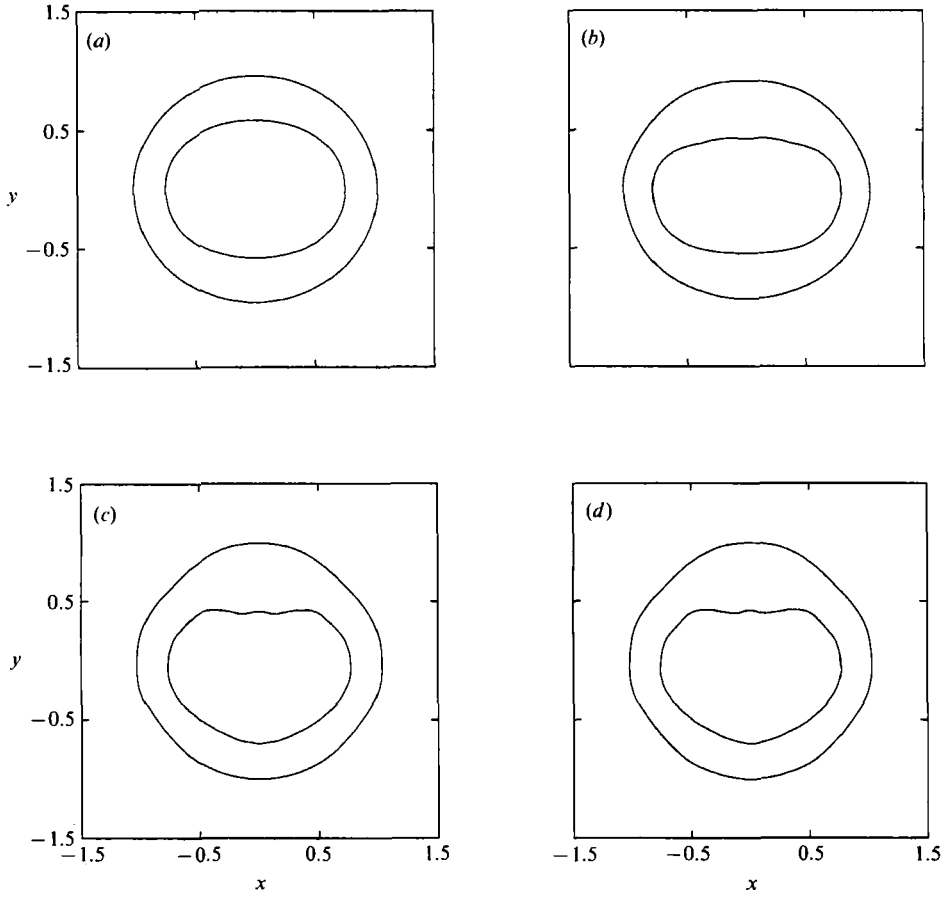

FIGURE 3. Shapes of an oscillating shell at $t = 2.2$ for (*a*) $\epsilon = 0.05$ and 40 elements per surface; (*b*) $\epsilon = 0.1$ and 40 elements; (*c*) $\epsilon = 0.15$ and 40 elements and (*d*) $\epsilon = 0.15$ and 60 elements per surface. In case (*c*) computations collapse a little after this time.

It is concluded that for large deformations and long integration times, high modes will inevitably appear. This simply means that the discretization required to capture the details of the solution makes the cost of very long computations prohibitive. In addition, these modes are going to be more strongly damped out by viscosity, which makes any further expenditure towards resolving them rather unnecessary.

Throughout the calculations it was made certain that the boundary shapes were accurate up to and including the second significant digit. Global accuracy was guaranteed by monitoring the invariants of the motion. For example, the total outflux was never larger than 10^{-5} and the total energy and the location of the centre of mass remained constant up to the fifth and fourth significant digits, respectively.

In the remaining part of this paper it should be understood, unless otherwise specified, that 40 elements are used for each of the interfaces. A time step $\Delta t = 0.002$ and 0.01 is used for the bubble mode and the sloshing mode, respectively, which results in 440 and 280 time steps per period of the second Legendre mode. For this discretization, 9.0 and 5.5 CPU hours are needed per period on an IBM 3084 for the bubble mode and sloshing mode, respectively. On the average, the CPU time decreased by a factor of three, when the IBM 3090 at Cornell University was used.

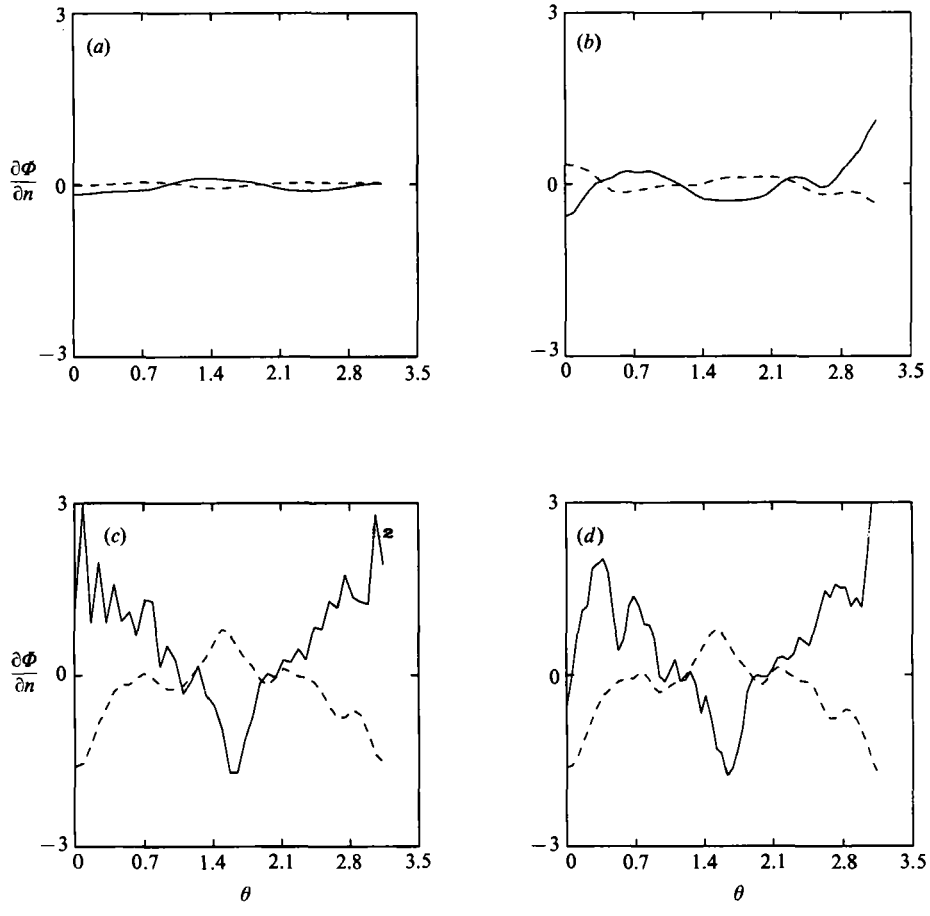

FIGURE 4. Normal derivative of the potential at the inner surface, $-\partial\Phi/\partial n_1$ (——) and at the outer surface, $\partial\Phi/\partial n_2$ (– – – –) at $t = 2.2$ for (*a*) $\epsilon = 0.05$ and 40 elements per surface; (*b*) $\epsilon = 0.1$ and 40 elements; (*c*) $\epsilon = 0.15$ and 40 elements and (*d*) $\epsilon = 0.15$ and 60 elements per surface.

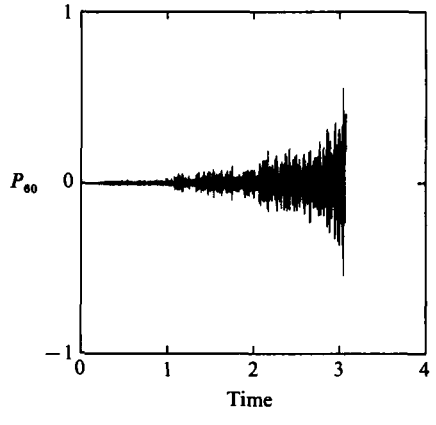

FIGURE 5. Amplitude of 60th mode of the flux through the inner surface for $\epsilon = 0.15$ and 60 elements per surface.

About 90% of the CPU time is consumed in setting up the system matrix and the remaining 10% to factorize it. By doubling the number of nodal points, the computation time is approximately tripled. This dependence is much weaker than the $O(N^3)$ increase that would have been observed if matrix inversion were the most time consuming part of the code. Moreover, construction of the system matrix requires a less than $O(N^2)$ increase in arithmetic operations owing to the concentrated numerical effort in elements surrounding the singular point. In all cases, the present formulation proceeded without resorting to out-of-core solvers.

7. Numerical results and discussion

7.1. *Linear oscillations*

Infinitesimal and moderate-amplitude oscillations of fluid shells were analysed by Saffren *et al.* (1982) and Tsamopoulos & Brown (1987), respectively, when the bubble is considered to be incompressible. The eigenvectors for any mode are given as equation (28) in the latter publication; whereas the linear dispersion relation for the eigenfrequency is repeated here for completeness:

$$\omega_n^2 = (n-1)(n+2)[(n+1)(1+R^{2n+4})+n(R^3+R^{2n+1})\pm(S_n)^{\frac{1}{2}}]/[2R^3(1-R^{2n+1})], \tag{7.1a}$$

where

$$S_n = (n+1)^2R^{4n+8}-2n(n+1)R^{4n+5}+n^2R^{4n+2}+2n(n+1)R^{2n+7}$$
$$+2(6n^2+6n+1)R^{2n+4}+2n(n+1)R^{2n+1}+n^2R^6-2n(n+1)R^3+(n+1)^2. \tag{7.1b}$$

Compressibility will modify only the zeroth mode. It can be shown that the dispersion relation for this mode is

$$\omega_{0,c}^2 = (6P_1\gamma R-2-2R^4)/(R^3-R^4). \tag{7.1c}$$

Numerical solution of the linear problem is particularly simple, since the discrete equations are also linear and can be solved by a single matrix inversion. Furthermore, if a constant time step is used, the system matrix to be inverted is unchanged. Thus, one matrix inversion is needed and is followed up by multiplication with a vector at every time step, resulting in minimal CPU time and storage.

Linear oscillations of a shell with $R = 0.7$ were computed using 40 elements for each surface and a time step of $\Delta t = T_2/400$, where $T_2 = 2\pi/\omega_2 = 0.858359$ is the linear period of the second bubble mode. Integration was carried out for 10 periods. The results at the end of the computations are accurate up to the fourth, third and second significant digit for the shape, potential, and flux, respectively. There is a slight deterioration of the accuracy of the results with increasing time, probably due to interaction of the two major modes with higher ones which are present in the form of round-off error. The evolution of the second Legendre coefficient of the shape of the inner and outer interface is shown in figure 6. By counting the maxima of the oscillations, the period may be recovered up to three significant digits, thus confirming the accuracy of the results. The total energy is conserved up to the sixth digit. The period of oscillation of the kinetic and dynamic energy is exactly half that of the second Legendre mode, as expected (Tsamopoulos & Brown 1983). Selected shapes and the energy evolution are given in Pelekasis (1991).

7.2. *Bubble mode*

As mentioned earlier, the primary motivation for this study is to identify and explain

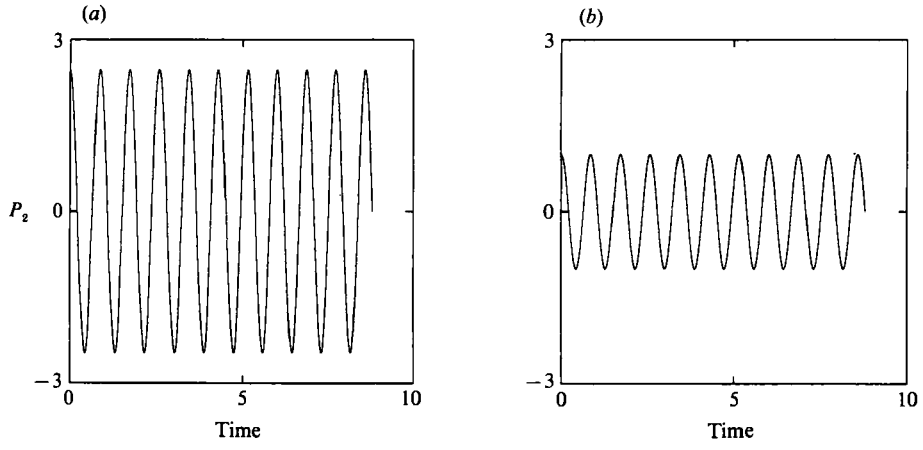

FIGURE 6. Linear amplitude of 2nd mode of the shape of the (*a*) inner and (*b*) outer interfaces.

the centring mechanism observed experimentally. The bubble is taken to be incompressible at first. In order to establish the connection with the earlier asymptotic analysis, the motion is initiated according to (2.9)–(2.10). Of course, this will only be correct up to $O(\epsilon^2)$, but even for the nonlinear formulation the mode of oscillation that exists initially prevails for quite some time.

Figure 7 shows the evolution of the two free surfaces in the bubble mode for about 14 periods of P_2. The initial disturbance is $\epsilon = 0.1$ and $R = 0.7$. A gradual increase of higher modes can be observed. This effect is even more pronounced in the flux. Moreover, as time integration proceeds, the two surfaces do not move completely in phase, but rather oscillate in a combined mode which consists of both bubble and sloshing modes. The evolution of the kinetic, surface and total energy is presented in figure 8. The total energy is conserved, whereas the kinetic and surface energy oscillate with half the period of the P_2 oscillations. Towards the end of the computation, variations in kinetic and dynamic energies become less regular owing to the presence of higher modes.

Figure 9(*a*) presents the location of the centre of mass of the drop and bubble along the axis of symmetry. The centre of mass of the shell remains constant (it is an invariant of the motion), but is slightly displaced from zero owing to $O(\epsilon^3)$ error in the initial disturbance. The two other centres oscillate in-phase around the centre of mass of the shell, in what is to be called from now on 'the slow oscillation' as opposed to the 'fast oscillation' of the P_2 mode.

This is a result of the nonlinear interplay between pressure and surface-tension forces. Surface tension tries to make each interface independently spherical. A displacement of the bubble towards the north pole of the drop, for example, forces fluid to move away from the upper portion of the shell. The small shell thickness induces higher velocities at the top as compared to those in the bottom, and, consequently smaller pressures according to Bernoulli's law. In the next phase of the motion, the higher pressure in the bottom forces the fluid to move upwards and thus the bubble is forced to move downwards. Simultaneously, the pressure in the bubble is uniform, although it may vary in time, whereas the pressure in the liquid varies as stated above. Therefore, the pressure drop across the interface of the bubble varies and must be counterbalanced by variations in the surface curvature. This last effect makes the bubble and the drop surface become less smooth. There is no indication

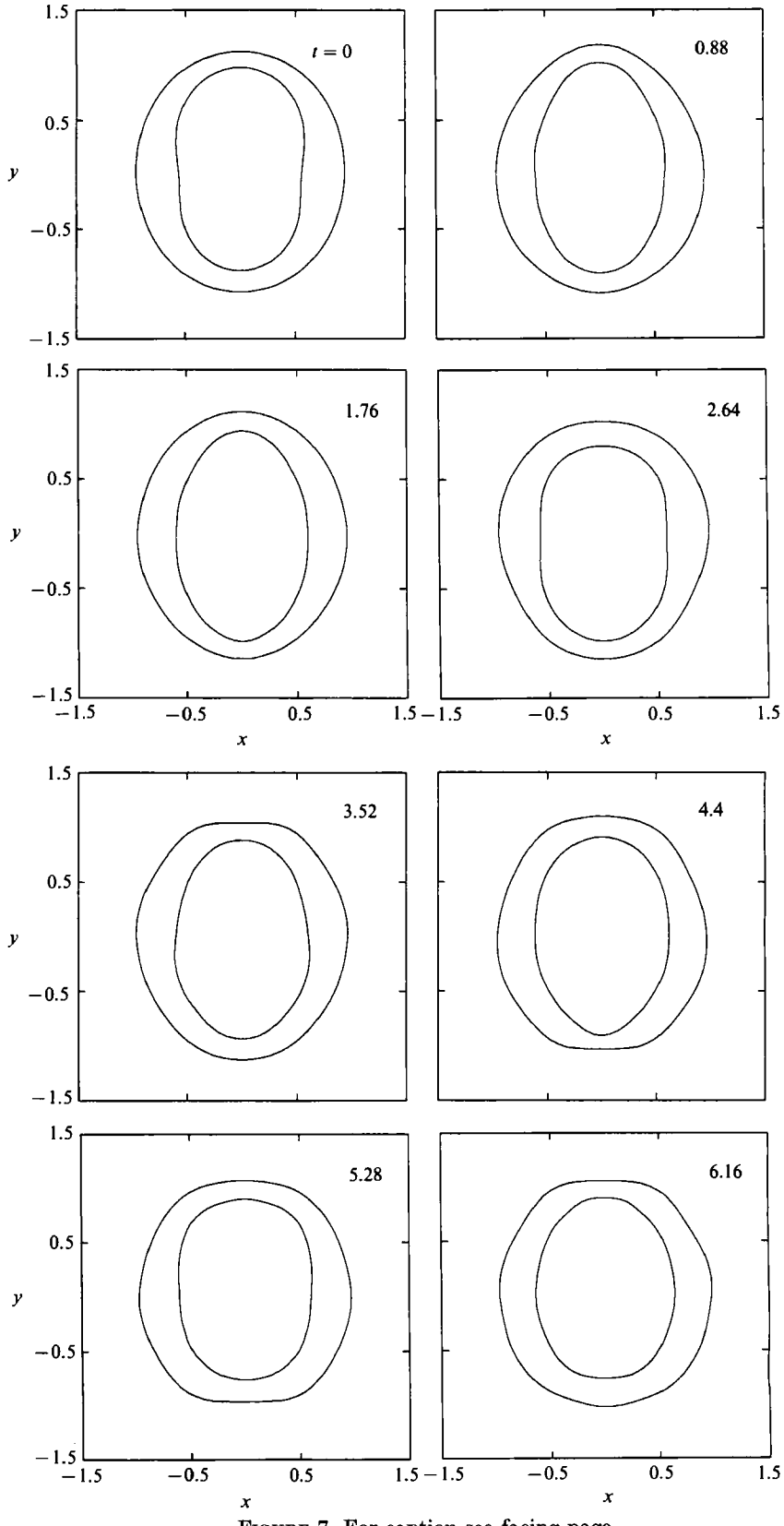

FIGURE 7. For caption see facing page.

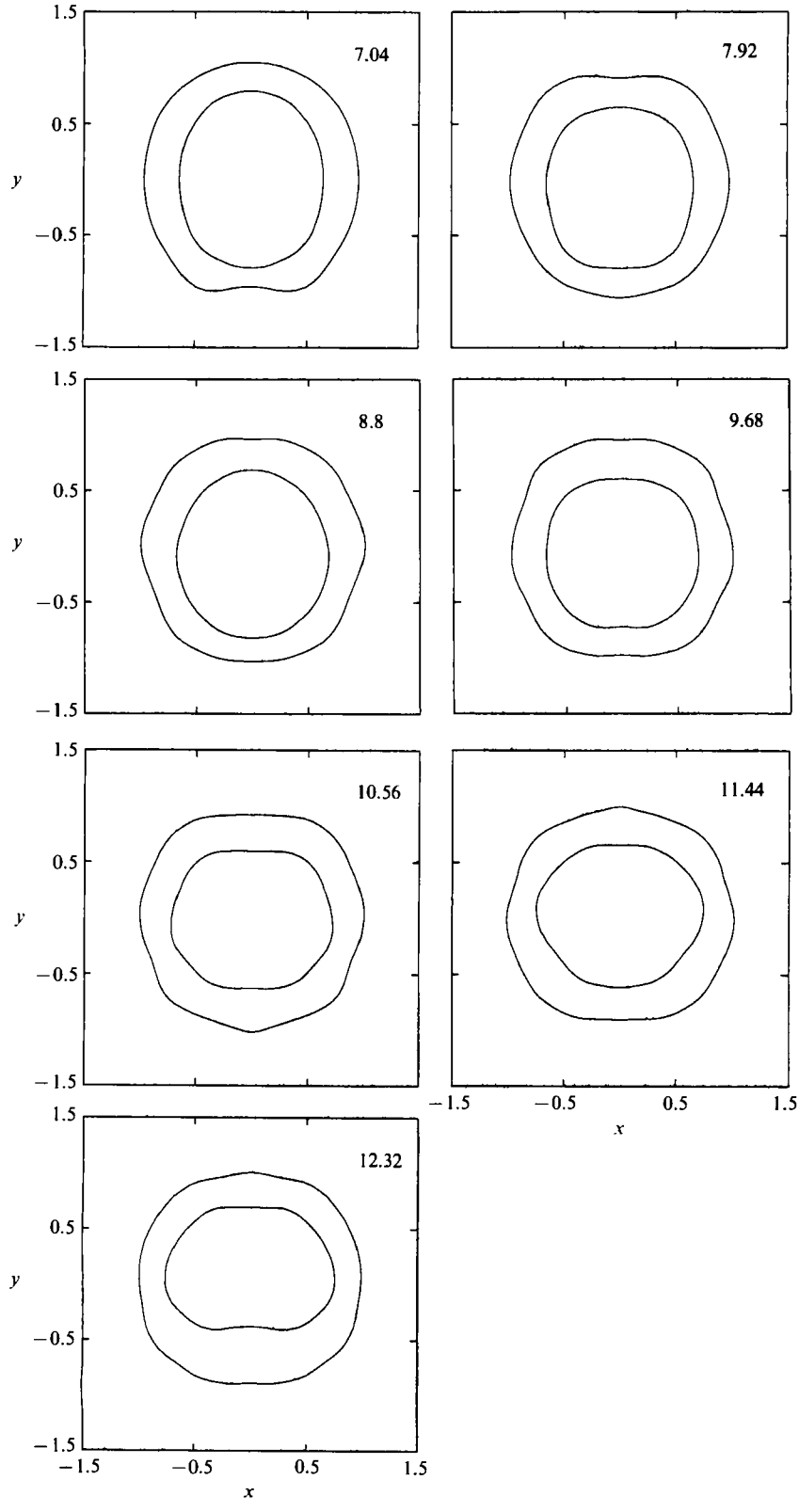

FIGURE 7. Shapes of a liquid shell oscillating in the bubble mode for 14 periods of the 2nd mode with $\epsilon = 0.1$ and $R = 0.7$ at the times shown on the plots. The nonlinear period of the fast oscillation for these parameters is roughly 0.88.

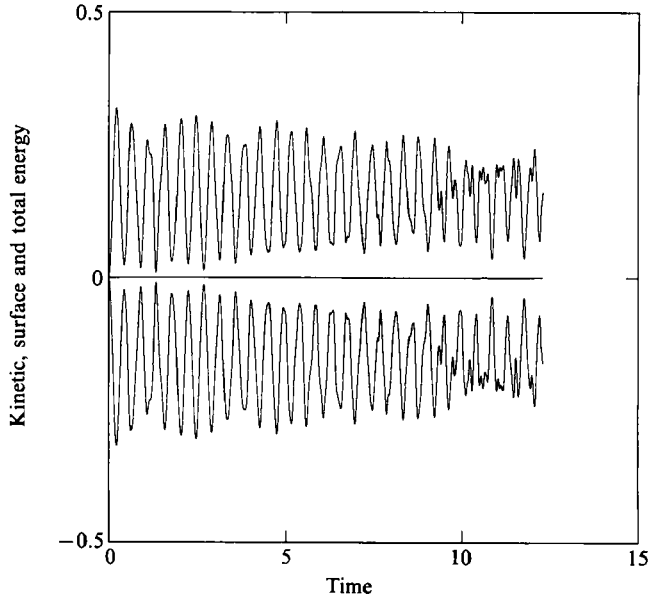

FIGURE 8. Surface, kinetic and total energy for a shell oscillating in the bubble mode with $\epsilon = 0.1$ and $R = 0.7$. The surface energy has been translated in such a way as to make the total energy zero. Positive values correspond to kinetic energy and negative ones to surface energy.

that the shell will become permanently concentric in the absence of viscosity. In fact, the amplitude of the slow oscillation seems to increase in time. This is probably due to transfer of energy to the first mode from higher ones.

Even though the motion is not strictly periodic, a period of the fast oscillation of P_2 and the other shape modes may be estimated by counting the peaks in their oscillations. For better accuracy, the shape of the outer surface is decomposed into Legendre–Fourier modes. The numerical error is smaller in the outer surface, since the initial deformation is not as severe owing to its larger radius. In the same way, the period of the slow oscillation is calculated. Clearly, it corresponds to the induced variation of the first Legendre mode of each surface. For $\epsilon = 0.1$, $R = 0.7$ and considering the first two peaks, it is found that the period of the fast oscillation is $T_f = T_2 = 0.886$ and that of the slow oscillation is $T_s = 5.472$. As time increases, the periods change owing to the presence of other modes. More specifically, the slow oscillation period increases to 6.8 after the third peak. Integration is halted at that point owing to deterioration of the accuracy of the solution.

The effect of the ratio of the two radii is studied next. R is a measure of the thickness of the shell and values of 0.7, 0.8 and 0.9 are used. The amplitude was kept at $\epsilon = 0.1$. The period of P_2 is very close to the one predicted by linear theory, whereas the period of the slow oscillation increases with increasing R. Shapes of shells are given in Pelekasis (1991). Figures 9(*b*) and 9(*c*) show the slow oscillation for $R = 0.8$ and 0.9, respectively. The period of the slow oscillation cannot be easily identified, because more than one peak exists, especially for $R = 0.8$ and 0.9. When $R = 0.9$, the slow oscillation is decelerated to the extent that after integrating for about 12 periods of the fast mode, the two centres of mass still have negative deviations from the centre of the shell. Further integration in time is impossible owing to loss of accuracy. The motion of the centres shown in figure 9(*c*) resembles the prediction of Tsamopoulos

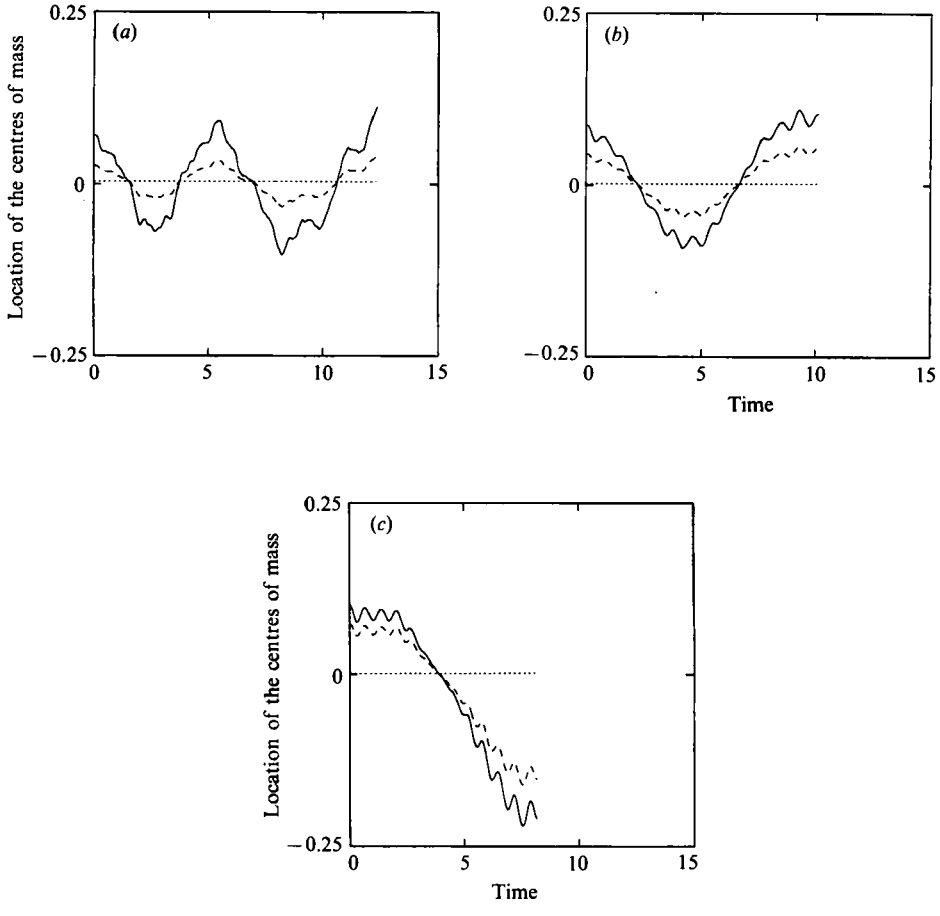

FIGURE 9. Bubble mode oscillations of the centres of mass of the bubble (——), the drop (– – –) and the shell (· · · ·) for (*a*) $\epsilon = 0.1$, and $R = 0.7$, (*b*) $\epsilon = 0.1$ and $R = 0.8$ and (*c*) $\epsilon = 0.1$ and $R = 0.9$.

& Brown (1987) for the first three periods of the fast mode (see their figure 6), namely, the period is that of the P_2 mode and the amplitude is nearly constant in time. As time increases further, higher nonlinear effects enter the picture and induce a movement of the bubble centre towards the concentric configuration. The reason for this close correspondence between the present numerical results and the weakly nonlinear theory is the increase of R for the same ϵ. This leads to bubble shapes that are closer to spherical. Similarly, the deceleration of the slow oscillation with increasing R can be explained. The weaker initial deformation results in a smaller surface tension and pressure variation in the shell, which are the major restoring mechanisms. Thus, the time needed for the surface tension force to become significant is longer and the period of the slow oscillation larger. On the other hand, if the ratio of the radii gets very small, the dynamics of the two interfaces will become decoupled and the centring mechanism will be delayed also. Therefore, there must be an optimum value of R for which the period of the slow oscillation attains a minimum. Landman (1985) reached similar conclusions in studying viscous compound drops.

Next, the effect of increasing amplitude on the period of oscillation was determined

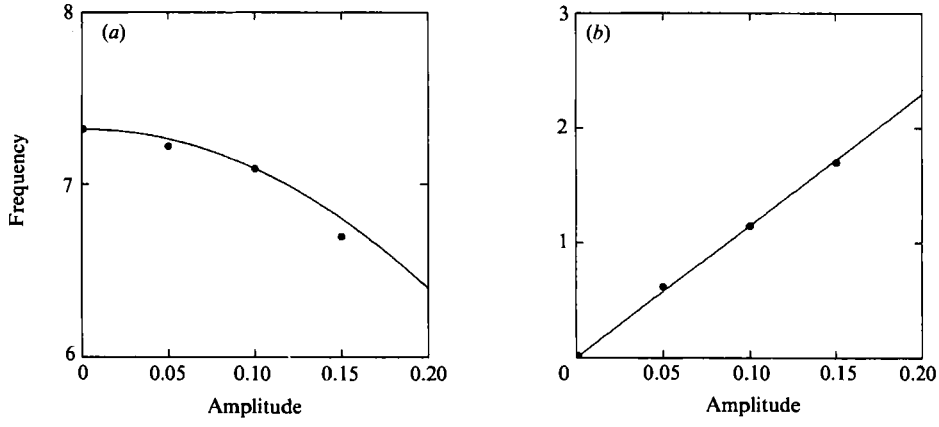

FIGURE 10. Frequency variation of (*a*) the fast oscillation and (*b*) the slow oscillation, with increasing amplitude of the initial distortion mode $P_2(\theta)$, in the bubble mode of oscillation. The dots correspond to numerical results.

Initial disturbance, ϵ	Frequency of fast oscillation $\omega_{2,b}$	Frequency of slow oscillation $\omega_{s,b}$
0	7.323	0
0.05	7.222	0.616
0.10	7.092	1.149
0.15	6.698	1.698

TABLE 1. Effect of amplitude of disturbance on oscillation frequencies in the bubble mode

by repeating the computations with $\epsilon = 0.05$ and 0.15. Numerical discretization and R are kept the same, and the results are given in figure 10 and table 1. Selected shapes are given in Pelekasis (1991). Results obtained for the fast oscillation are in agreement with those obtained by Tsamopoulos & Brown (1987). Specifically, an approximately quadratic decrease of the frequency of the second bubble mode with increasing ϵ is observed:

$$\omega_{2,b} = 7.323 - 23.1\epsilon^2. \tag{7.2a}$$

This is expected, since the increased inertia in the nonlinear model decelerates the motion. The value obtained for $\epsilon = 0.15$ does not quite follow the ϵ^2 rule, but, as pointed out earlier, larger values of ϵ result in a faster increase of the high modes, and dispersion of energy to them.

The frequency of the induced slow oscillation is approximately proportional to ϵ, which indicates a strongly nonlinear effect:

$$\omega_{s,b} = 11.49\epsilon. \tag{7.2b}$$

This is due to the fact that, for larger ϵ, more energy is allowed to transfer to the first Legendre mode, resulting in acceleration of the slow oscillation. In addition, this result is in agreement with the findings of Lee & Wang (1988) for thin shells. Tsamopoulos & Brown (1987) do not predict such a behaviour for the bubble mode. They carried out a weakly nonlinear analysis up to third order and they found that the oscillation of both the bubble and drop centres will be of constant amplitude. In

addition, they predicted that the centres will never become identical to the shell centre. A possible explanation for this difference is that the numerically calculated results are correct to all orders of ϵ, and indicate a very long period for the slow oscillation which cannot be predicted analytically unless additional slower timescales are introduced in the multiple-scales expansion.

7.3. *Sloshing mode*

A similar investigation is carried out for the sloshing mode. Figure 11 presents the evolution of shapes over seven periods of P_2. The initial disturbance and R are 0.15 and 0.7, respectively. It is observed that the P_2 mode primarily determines the shape of the shell throughout the motion. In figure 12 the surface, kinetic and total energy are shown. They do not exhibit any significant departure from those of a steady oscillation.

The motion of the centres of mass is plotted in figure 13, exhibiting a slow oscillation around the centre of mass of the shell, which they reach simultaneously. This is another indication of the high accuracy of the present calculations. The slow period is about 8.6 and the centre of mass of the shell remains stationary and close to zero. This is a picture very similar to the one obtained for the bubble mode. Again, there is no indication of achieving the concentric configuration permanently in the absence of viscosity. Figure 14 presents the evolution of some of the Legendre–Fourier modes of the shape of the outer surface. The second mode is the dominant one.

A good estimate of the nonlinear frequencies of the different modes is obtained by enumerating the peaks in the oscillations. This was performed for $\epsilon = 0.1$, 0.12, 0.15 and 0.2. Shapes of shells are given in Pelekasis (1991). When $\epsilon = 0.2$, integration cannot proceed beyond half a period of P_2 because the two surfaces touch each other. This does not allow the study of short-wavelength instability in the sloshing mode of oscillation. The same behaviour has been reported by Lee & Wang (1988). Using data from the other three cases, figure 15 and table 2 were prepared. It is observed that the period (frequency) of the second mode increases (decreases) quadratically with ϵ as predicted by Tsamopoulos & Brown (1987):

$$\omega_{2,s} = 2.285 - 5.56\epsilon^2. \tag{7.3a}$$

The period of the induced slow oscillation is again inversely proportional to ϵ, which is in agreement with the results of Lee & Wang (1988):

$$\omega_{s,s} = 4.67\epsilon. \tag{7.3b}$$

Tsamopoulos & Brown (1987) predict centring during oscillation in the sloshing mode, which will eventually lead to a concentric configuration. This difference is probably due to a higher-order effect that the weakly nonlinear theory is unable to capture.

Increasing R to 0.8 results in touching of the two surfaces for a lower value of ϵ, namely 0.1. By decreasing ϵ to 0.08, this is avoided and integration for more than one period of the slow oscillation is carried out. The slow oscillation is shown in figure 16 and exhibits a period of 21.74. By extrapolating the results for $R = 0.7$ to the value $\epsilon = 0.08$, the slow period is expected to be $T_s = 16.8$, which is significantly smaller than the period found for $R = 0.8$. This is a similar effect to the one observed for the bubble mode and it is due to the increase of R for constant initial deformation.

7.4. *Effects of gas compressibility*

When the gas in the bubble is considered to be compressible, its volume and

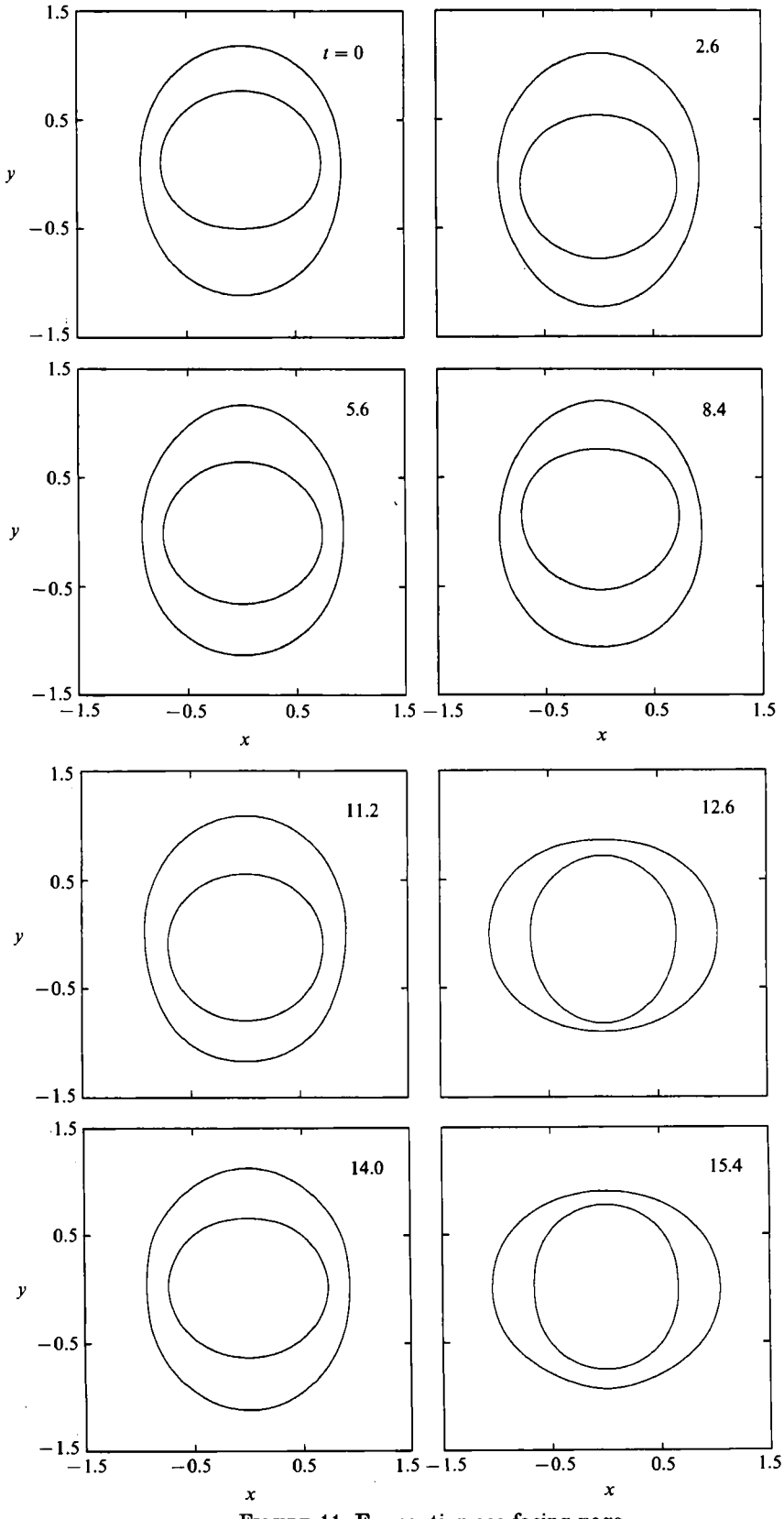

FIGURE 11. For caption see facing page.

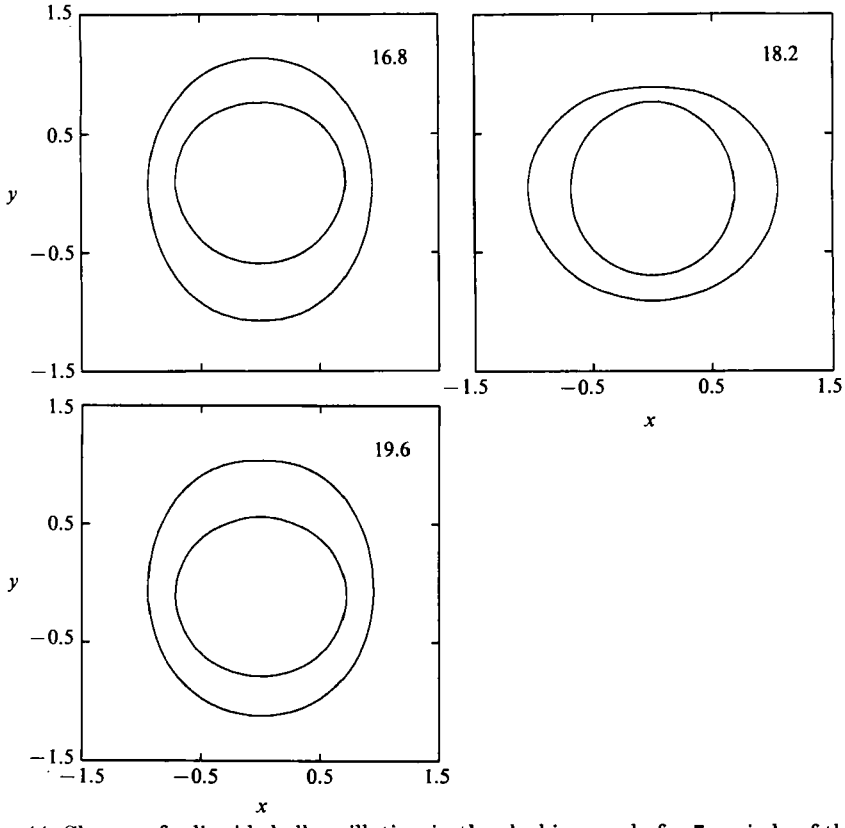

FIGURE 11. Shapes of a liquid shell oscillating in the sloshing mode for 7 periods of the 2nd mode with $\epsilon = 0.15$ and $R = 0.7$ at the times shown on the plots. The nonlinear period of fast oscillation for these parameters is roughly 2.8.

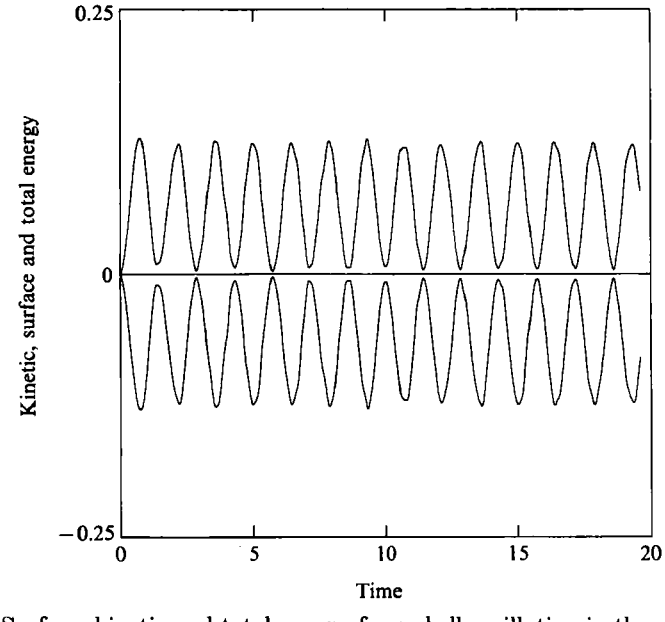

FIGURE 12. Surface, kinetic and total energy for a shell oscillating in the sloshing mode with $\epsilon = 0.15$ and $R = 0.7$. The surface energy has been translated in such a way as to make the total energy zero. Positive values correspond to kinetic energy and negative ones to surface energy.

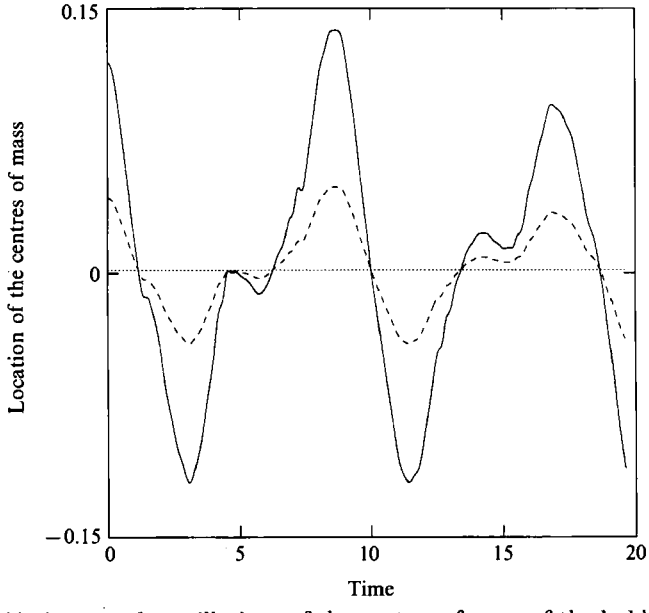

FIGURE 13. Sloshing mode oscillations of the centres of mass of the bubble (——), the drop (– – –) and the shell (· · · ·) for $\epsilon = 0.15$ and $R = 0.7$.

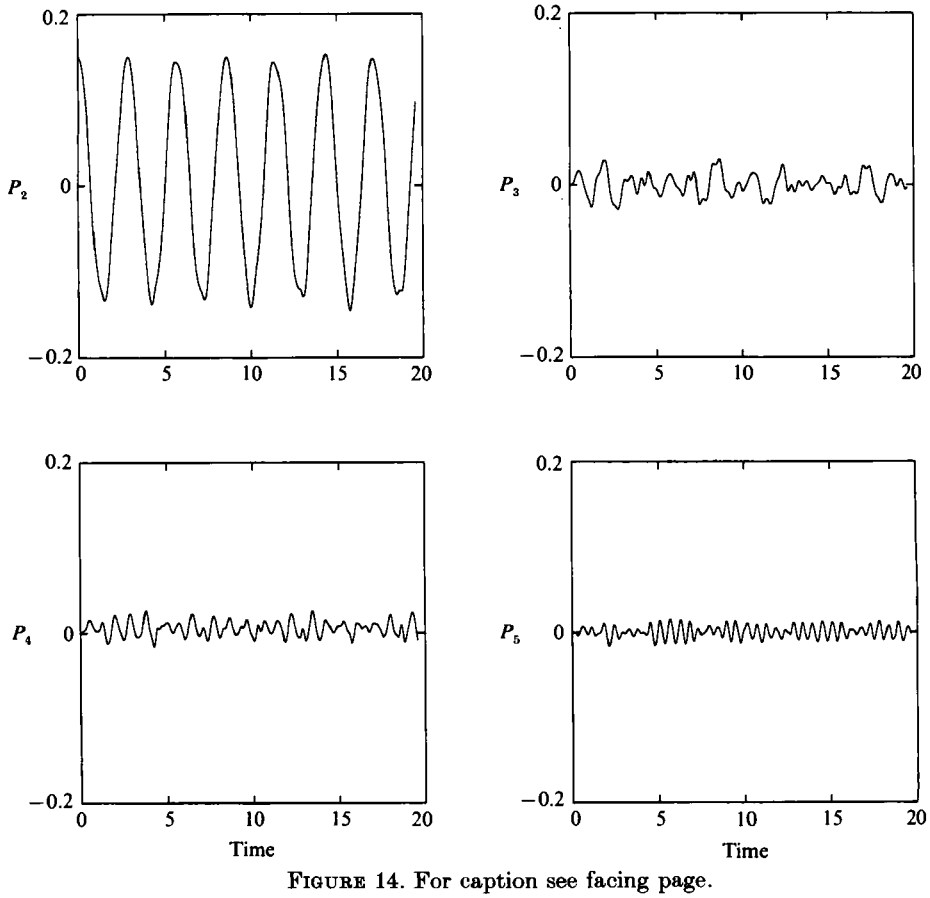

FIGURE 14. For caption see facing page.

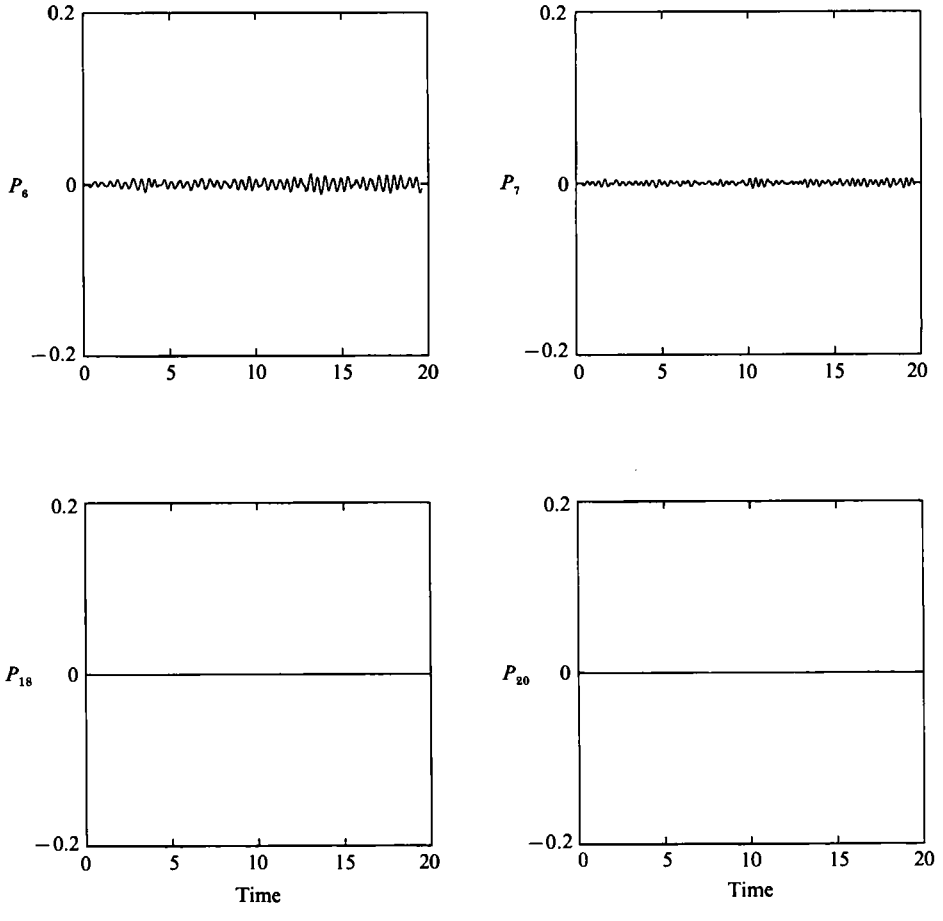

FIGURE 14. Amplitude of modes 2–7, 18 and 20 of the shape of the outer interface for a shell oscillating in the sloshing mode with $\epsilon = 0.15$ and $R = 0.7$.

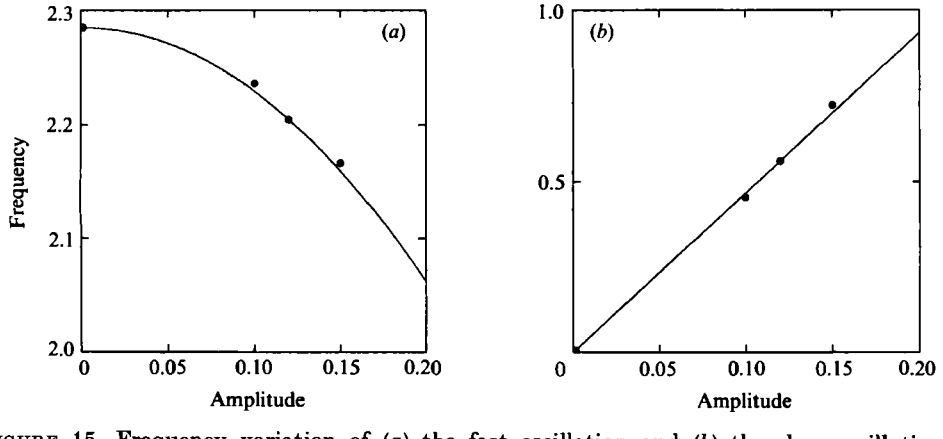

FIGURE 15. Frequency variation of (*a*) the fast oscillation and (*b*) the slow oscillation, with increasing amplitude of the initial distortion mode $P_2(\theta)$, in the sloshing mode of oscillation. The dots correspond to numerical results.

Initial disturbance, ϵ	Frequency of fast oscillation $\omega_{2,s}$	Frequency of slow oscillation $\omega_{s,s}$
0	2.285	0.0
0.1	2.236	0.455
0.12	2.205	0.560
0.15	2.167	0.724

TABLE 2. Effect of amplitude of disturbance on oscillation frequencies in the sloshing mode

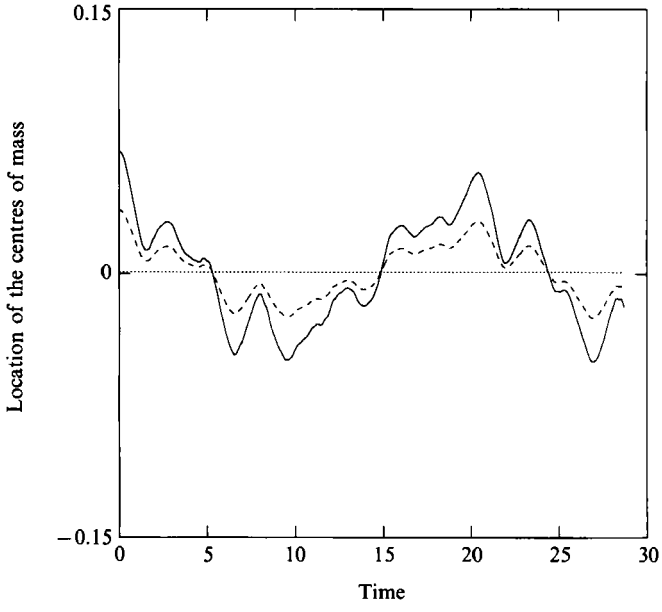

FIGURE 16. Sloshing mode oscillations of the centres of mass of the bubble (——), the drop (– – –) and the shell (· · · ·) for $\epsilon = 0.08$ and $R = 0.8$.

consequently the volume of the drop are allowed to vary in time, provided that the volume of the shell remains the same. This will take place irrespective of whether or not the volume of the bubble is altered initially, since it is a result of the dynamic interaction between pressure and surface tension on the interfaces.

Volume variations are equivalent to variations of the zeroth Legendre mode which was held constant in the incompressible case. In fact, Longuet-Higgins (1989*a*), in his asymptotic study of sound generation from oscillating axisymmetric gas bubbles, showed, to second order, that any of the distortion Legendre modes will induce pressure radiation that decays only like r^{-1} away from the bubble. If, in addition, the frequency of the originally excited mode happens to be half of that of the zeroth mode, there will be resonance between the two. Therefore, energy will be transferred very effectively to the zeroth mode and its amplitude will increase significantly.

It should be noted here that the possibility of resonance in drop dynamics had been analysed in some detail by Tsamopoulos & Brown (1984). In an earlier work by the same authors (Tsamopoulos & Brown 1983), weakly nonlinear oscillations of liquid drops and incompressible gas bubbles were considered. This was accomplished by following the methodology of Tadjbakhsh & Keller (1960). Clearly, in that case the zeroth mode is disallowed, and its frequency is purely imaginary (see also (7.1)). This

was also noted by Benjamin (1989), who argued that the monopole component can only arise from changes in the bubble's volume. These are the reasons for the form of the second-order solution given by Tsamopoulos & Brown (1983), in contrast to the conjecture of Longuet-Higgins (1989*a*). When the true initial-value problem was considered by Tsamopoulos & Brown (1984), terms of the form $(\omega_4^2 - 4\omega_2^2)$ did appear in the denominator of the solution and signalled the possibility of resonance between higher modes. Consequently, only when the gas in the bubble is considered compressible will the interplay of nonlinear terms in Bernoulli's equation and curvature bring about resonance with the zeroth mode (Longuet-Higgins 1989*b*).

Similarly here, if the gas in the bubble is considered to be compressible, resonance of the zeroth mode may be obtained. In particular, if $\epsilon = 0.1, R = 0.7$ and the bubble mode of oscillation is initially excited, its nonlinear period is approximately 0.88. Choosing $P_1(t = 0)$ to be 4.1725 in (7.1), the period of the zeroth mode is calculated to be 0.44. These values will induce resonance between the second and the zeroth modes. When the liquid in the shell is water and it is surrounded by air at atmospheric pressure, the dimensionless pressure required above corresponds to an outer radius of the order of microns. When higher modes are initially excited, the outer radius necessary for resonance is larger.

Figure 17 shows the evolution of the shell with time. These shapes are not much different from the ones obtained for an incompressible bubble, except for the variation in volume. Figure 18 shows the oscillations of the first seven Legendre modes of the shape of the outer surface, along with some high modes. The envelopes surrounding the oscillations of the zeroth and second Legendre modes indicate a slow exchange of energy between these two modes. A similar envelope is exhibited by the fourth mode. By counting the peaks, it was found that the period of the fourth mode is approximately 0.4, which allows for resonance between the fourth mode and either the second or the zeroth modes. The other modes behave quite regularly and the higher ones are almost non-existent. This behaviour is expected according to the analysis of Tsamopoulos & Brown (1984) and Longuet-Higgins (1989*a*).

In figure 19 the evolution of energy is presented. The total energy is again invariant and, besides the kinetic and surface energy, it includes the energy due to volume variations, which is not shown. The oscillations of the centres of mass are shown in figure 20. The period of the slow oscillation is found to be 5.3, which is somewhat smaller than 5.47 obtained when compressibility effects were excluded. In order to examine the reasons for this difference, calculations were carried out for the same parameters except that the internal pressure was initially set to 2.0. This value does not allow for resonance of the zeroth mode. Figures 21 and 22 show the oscillations of the Legendre modes and the centres of mass, respectively. The evolution of shapes is given elsewhere (N. Pelekasis 1991). The absence of resonance between the zeroth and the second mode is obvious, whereas the coupling between the fourth and the second mode is more pronounced in the oscillations of the fourth mode, now that there is no competition from the zeroth mode. The amplitudes of the oscillations of the zeroth and first mode are smaller when there is no resonance. Consequently, the oscillations of the centres of mass exhibit smaller amplitude and the period is the same as that obtained for the incompressible case. It can be argued that, when there is resonance between the zeroth and the second modes, there is a transfer of energy from the initially excited mode to the zeroth one. The zeroth mode in turn transfers energy to all the modes and, most importantly and quickly, to the first one which oscillates faster, resulting in smaller periods of oscillation of the two centres of mass.

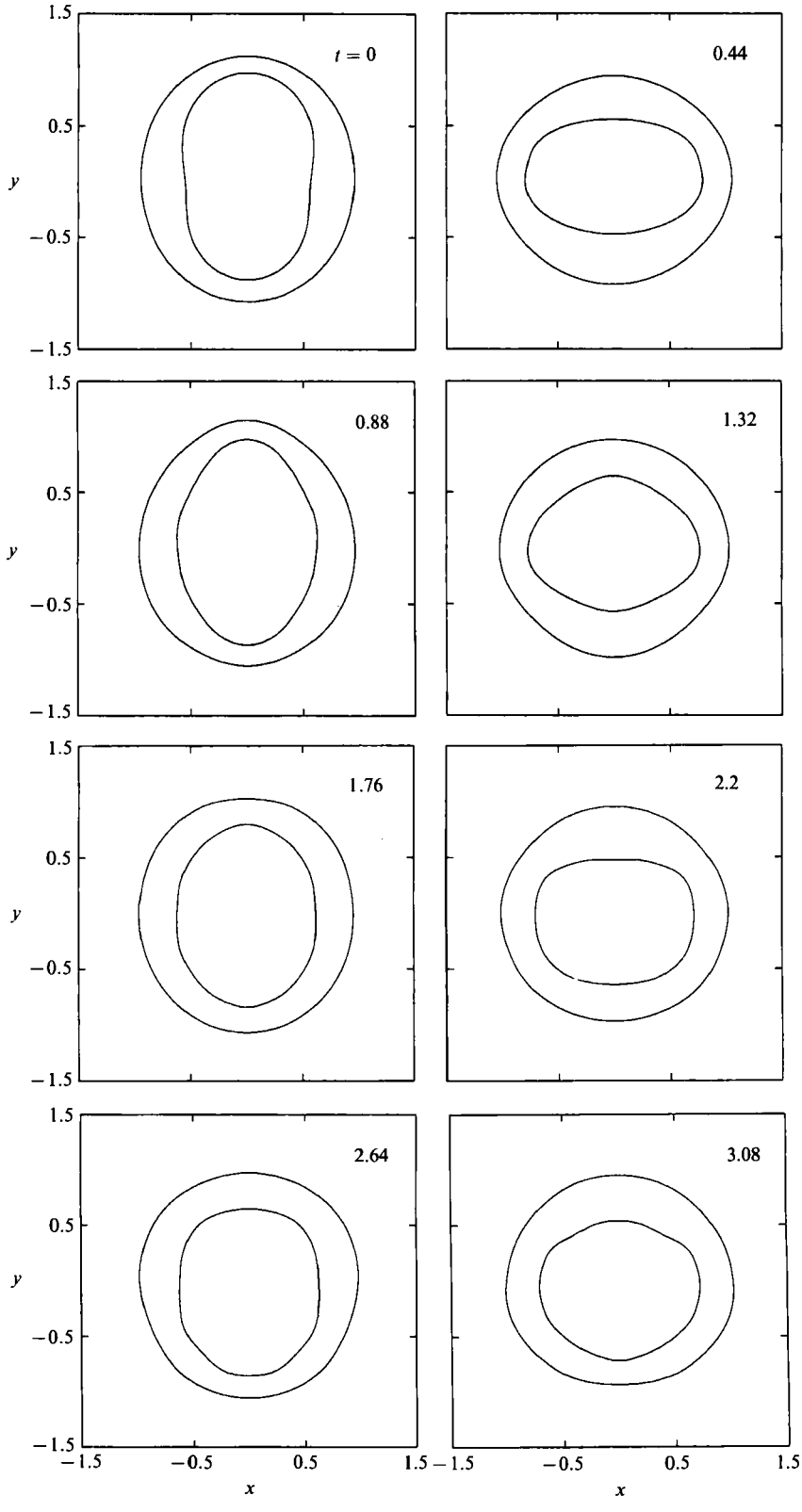

FIGURE 17. For caption see facing page.

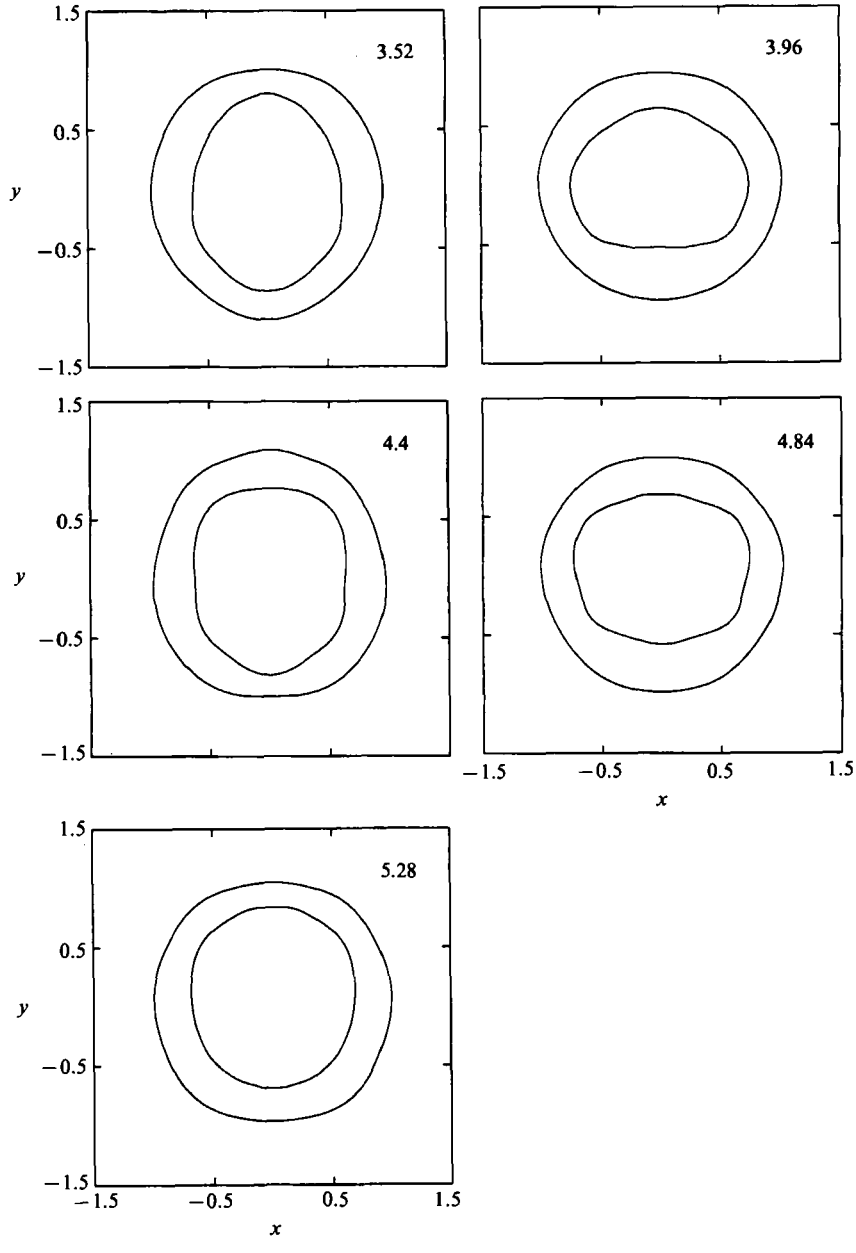

FIGURE 17. Shapes of a liquid shell surrounding a compressible bubble, oscillating in the bubble mode for 6 periods of 2nd mode with $\epsilon = 0.1$ and $R = 0.7$ at the times shown on the plots. The nonlinear period of fast oscillation for these parametric values is roughly 0.88 and it is equal to twice the period of the zeroth mode.

This analysis was repeated for the sloshing mode. It was found that, when resonance exists, the two surfaces touch each other before a single period of the second mode is completed. Specifically, for $R = 0.7$ and $\epsilon = 0.1$ the two surfaces touch at $t = 2.55$. This is happening because the amplitude of the oscillations

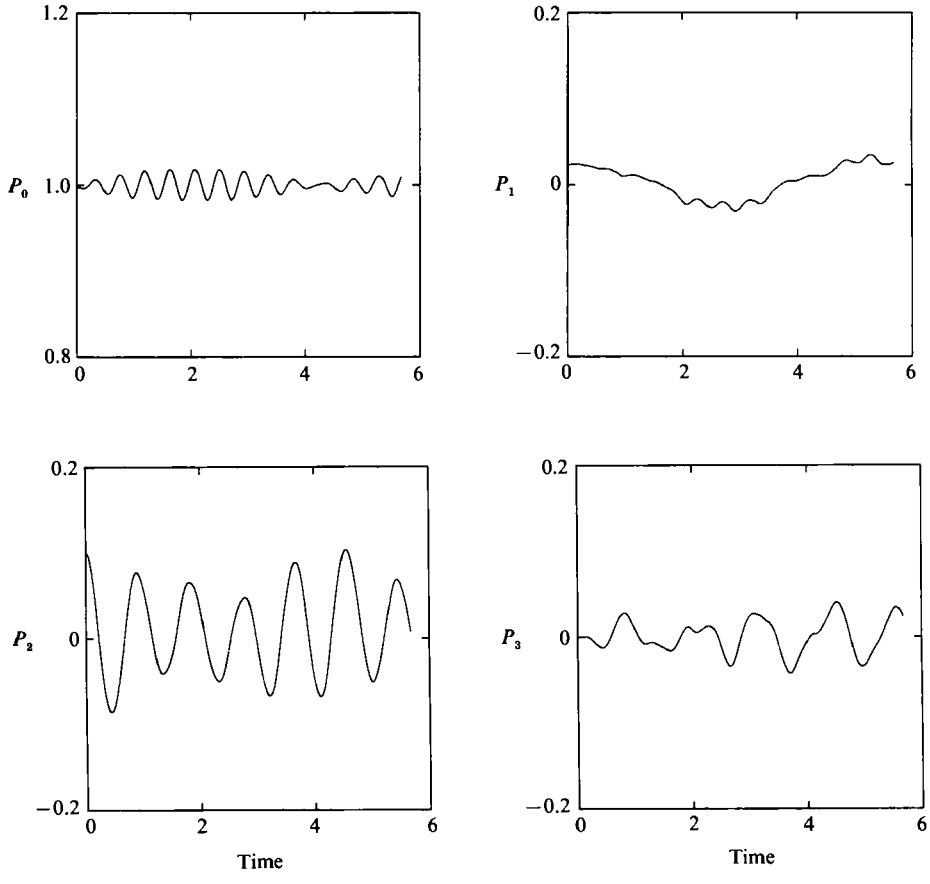

FIGURE 18. For caption see facing page.

increases and at the same time the two surfaces move out of phase. When the initial pressure inside the bubble is such that resonance is avoided, results similar to those for an incompressible bubble are obtained. This can be seen in figures 23 and 24. The period of the slow oscillation around the concentric configuration is 11.38, which essentially is the same as that found for the incompressible case.

7.5. *Effect of initial conditions*

In all cases presented so far, the centres of mass of the bubble and the drop are initially displaced in such a way that the centre of mass of the shell is fixed and very close to zero. Alternatively, the bubble alone may be initially displaced, thus setting the centre of mass of the shell further away from the zero value along the axis of symmetry. In this way, the magnitude of the shape oscillations is disassociated from the initial displacement of the centres of mass.

Such an initial disturbance is given by (2.11*a*) and (2.11*b*) with Δ being a measure of the initial displacement of the centre of mass of the bubble. The effect of Δ on the motion is tested by running cases with $\epsilon = 0.1$ and $R = 0.7$ with the shell oscillating in the bubble mode for two different values of Δ, namely 0.05 and 0.07. Evolution of shapes and the invariants of the motion are given elsewhere (N. Pelekasis 1991). The periods of the fast and slow oscillations for both cases are the same as those when the

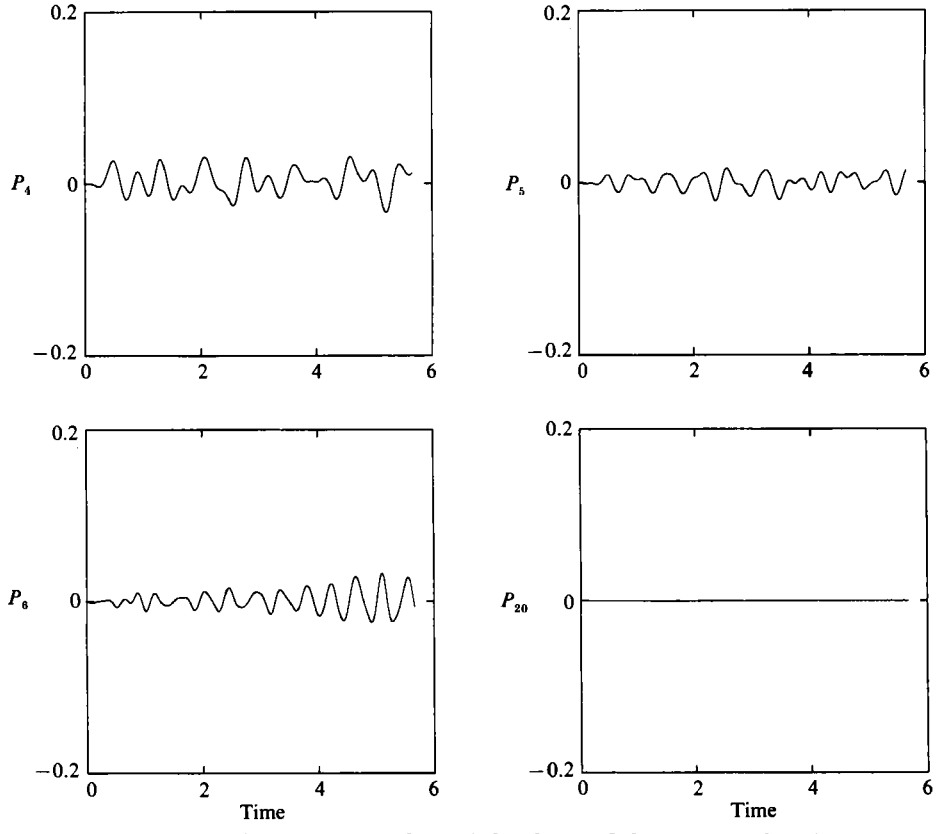

FIGURE 18. Amplitudes of modes 0–6 and 20 of the shape of the outer surface for a shell oscillating in the bubble mode with $\epsilon = 0.1$ and $R = 0.7$ with P_2 and P_0 in resonance.

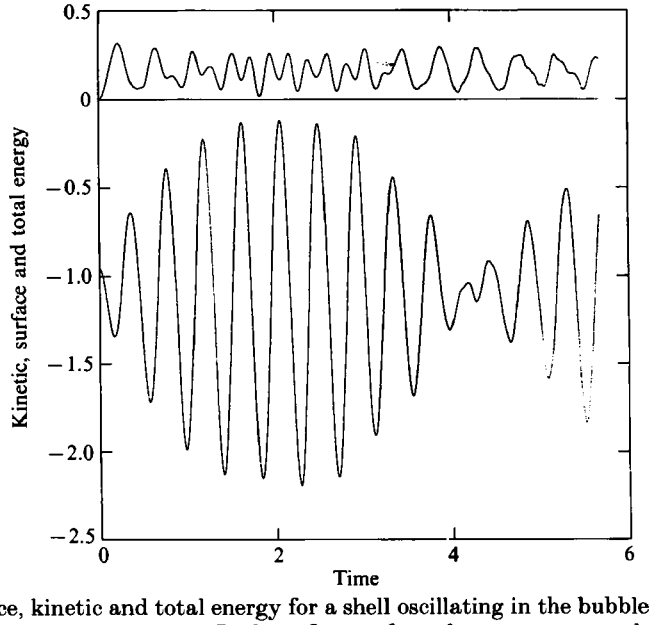

FIGURE 19. Surface, kinetic and total energy for a shell oscillating in the bubble mode ($\epsilon = 0.1$ and $R = 0.7$) with P_2 and P_0 in resonance. Both surface and total energy are translated independently since volume energy also contributes. Positive values correspond to kinetic energy and negative ones to surface energy.

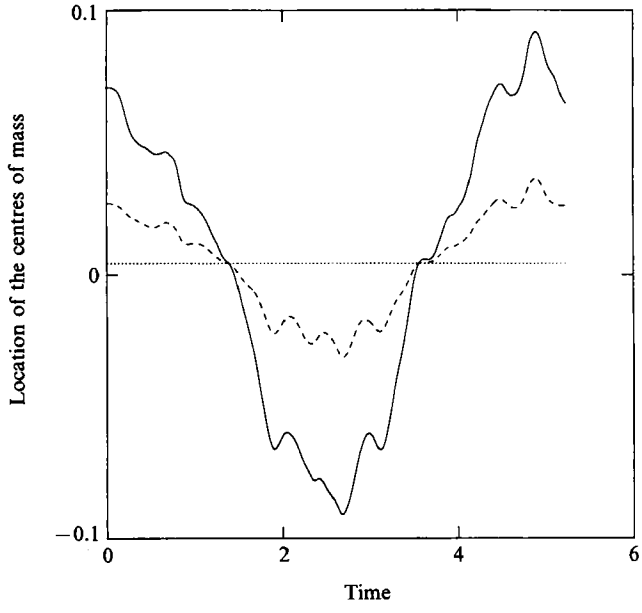

FIGURE 20. Bubble mode oscillations of the centres of mass of the bubble (——), the drop (– – –) and the shell (· · · ·) for $\epsilon = 0.1$ and $R = 0.7$ under resonance conditions.

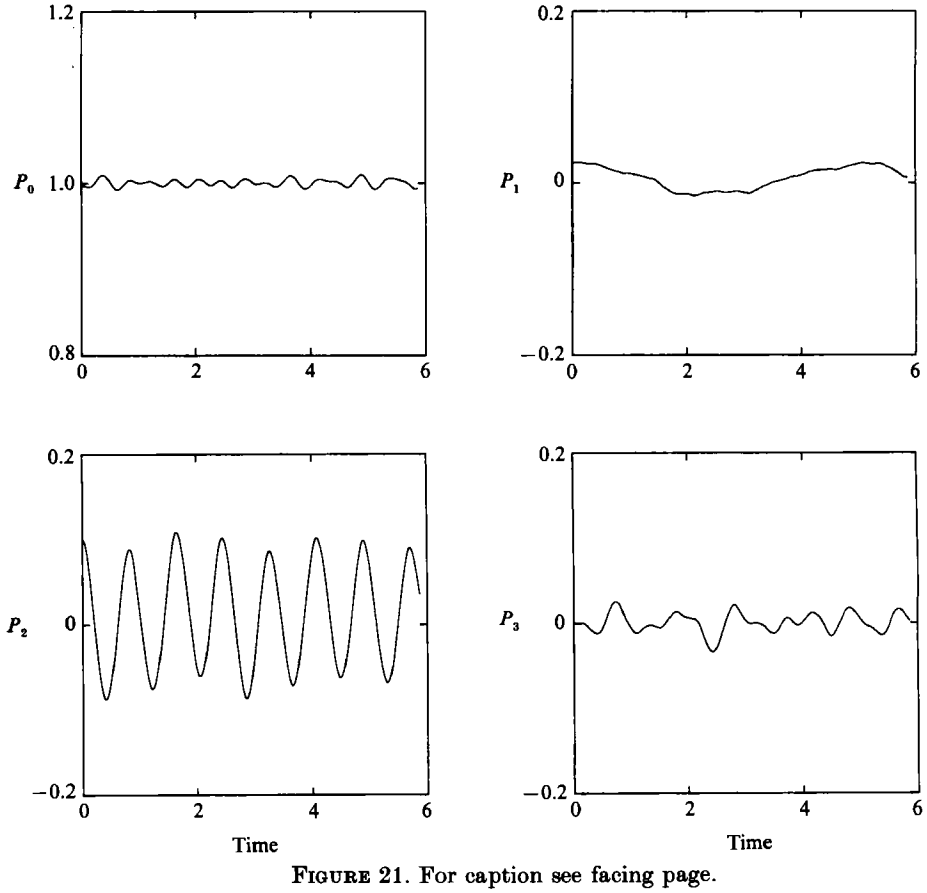

FIGURE 21. For caption see facing page.

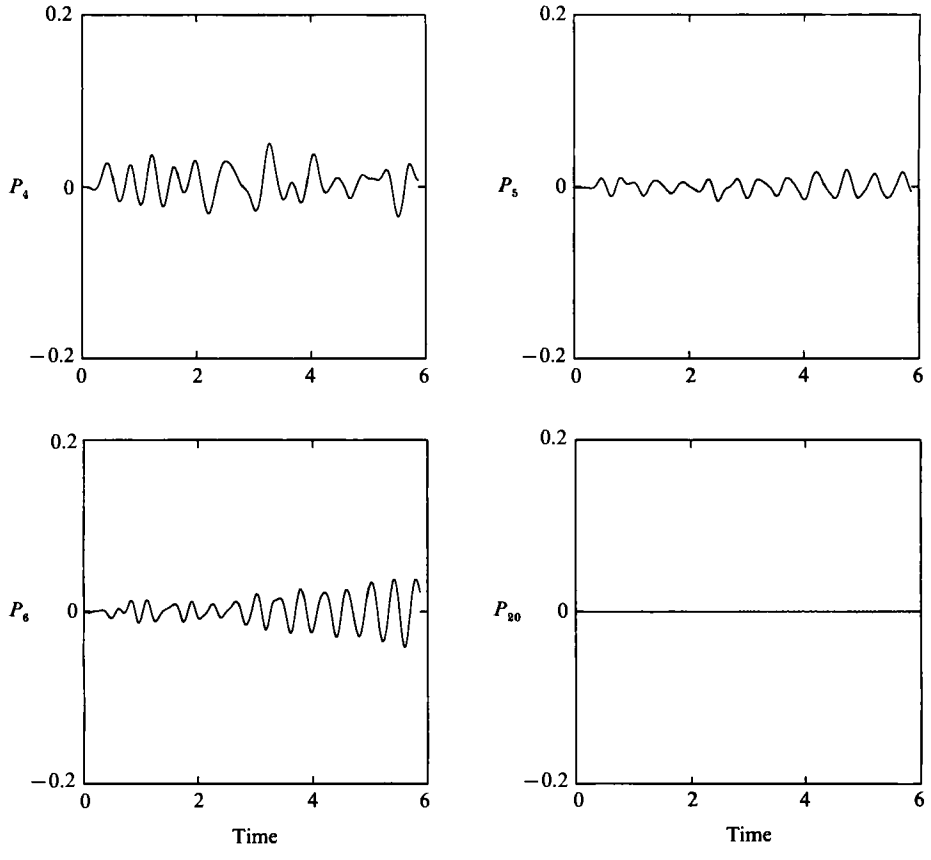

FIGURE 21. Amplitudes of modes 0–6 and 20 of the shape of the outer surface for a shell oscillating in the bubble mode with $\epsilon = 0.1$, $R = 0.7$ and away from resonance conditions.

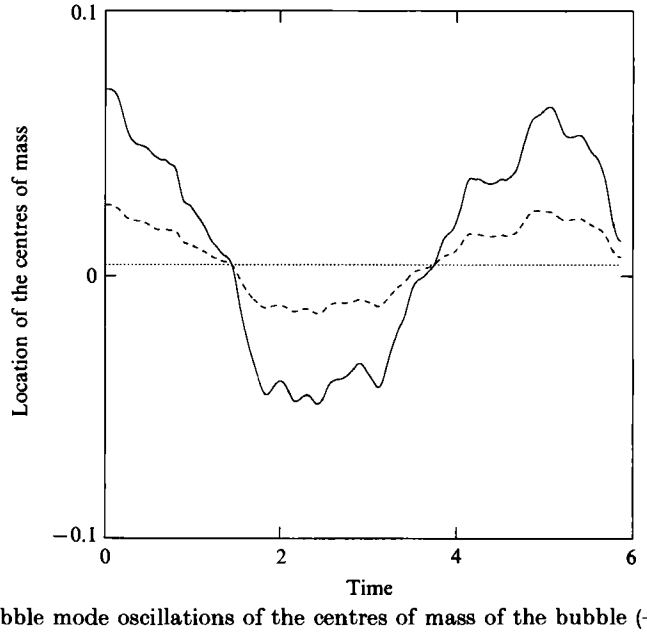

FIGURE 22. Bubble mode oscillations of the centres of mass of the bubble (——), the drop (– – –) and the shell (· · · ·) for $\epsilon = 0.1$, $R = 0.7$ and away from resonance conditions.

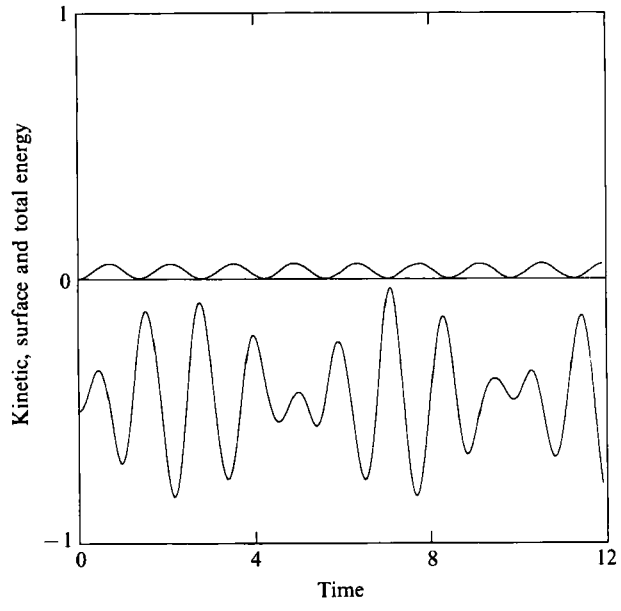

FIGURE 23. Surface, kinetic and total energy for a shell oscillating in the sloshing mode with $\epsilon = 0.1$, $R = 0.7$ and away from resonance conditions. Both surface and total energy are translated independently since volume energy also contributes. Positive values correspond to kinetic energy and negative ones to surface energy.

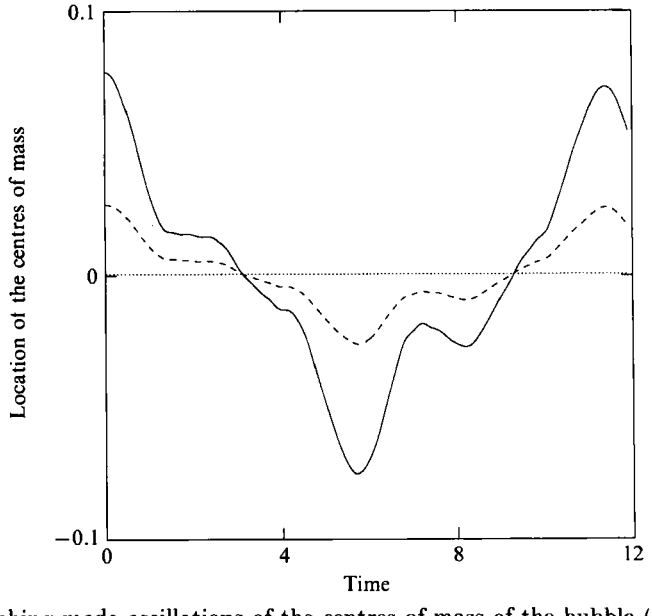

FIGURE 24. Sloshing mode oscillations of the centres of mass of the bubble (——), the drop (– – –) and the shell (· · · ·) for $\epsilon = 0.1$, $R = 0.7$ and away from resonance conditions.

centre of mass of the shell is set to zero. The same effect has been observed by Lee & Wang (1988) in the thin shell limit. Of course as Δ increases further, the north pole of the bubble approaches the corresponding one of the drop and the two surfaces touch each other sooner.

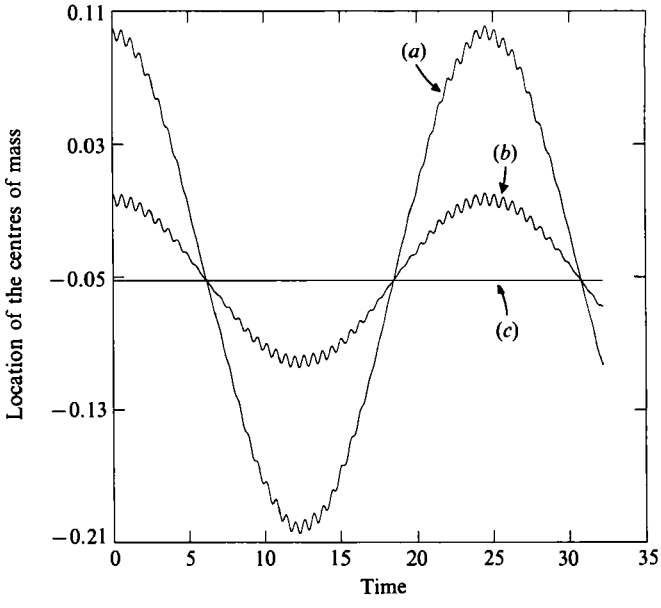

FIGURE 25. Oscillations of the centres of mass of (*a*) the bubble, (*b*) the drop and (*c*) the shell for $R = 0.7$, $\Delta = 0.1$, static internal gas pressure $P_1 = 2$ and external gas pressure 40% higher than the static value.

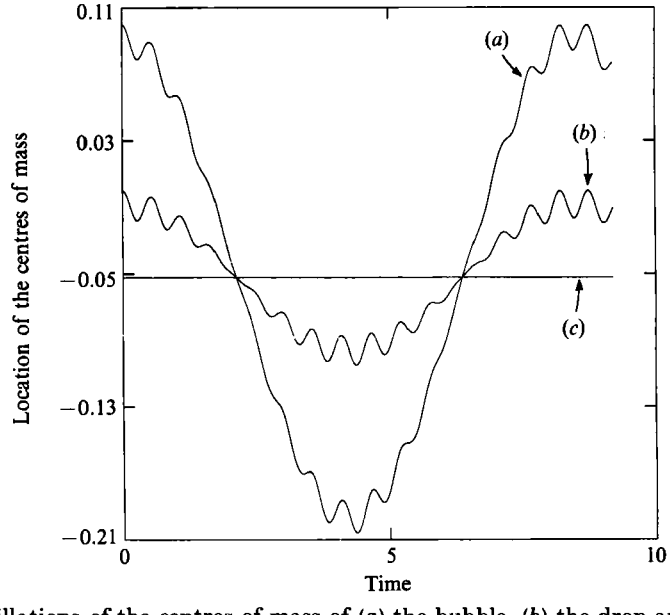

FIGURE 26. Oscillations of the centres of mass of (*a*) the bubble, (*b*) the drop and (*c*) the shell for $R = 0.7$ $\Delta = 0.1$, static internal gas pressure $P_1 = 2$ and external gas pressure 120% higher than the static value.

The third type of initial condition tested is given by (2.12). In this case, both interfaces are spherical and the shell is neutrally stable. However, a step change in the outer pressure induces volume oscillations in the bubble. For the purpose of the present calculations, $R = 0.7$, $P_1 = 2$, $\Delta = 0.1$ and the outer pressure was increased by either 40% or 120% from its original static value. Figures 25 and 26 show the slow

Percentage change in outer pressure from static value	Frequency of fast oscillation $\omega_{0,p}$	Frequency of slow oscillation $\omega_{s,p}$
0	9.50	0
40	10.33	0.257
120	11.55	0.757

TABLE 3. Effect of pressure disturbance on oscillation frequency of the shell

oscillation of the centres of mass of the bubble, the drop and the shell. It can be seen that the fast oscillation is again present and it corresponds to the zeroth mode. However, its amplitude is much smaller since no surface deformation modes were initially present, but arose through nonlinear coupling. For the same reason, calculations are not constrained by the appearance of numerical instabilities. Table 3 demonstrates that increasing the initial disturbance results in smaller frequency of the slow oscillation in accordance with the earlier cases. Finally, it is quite important to mention that the frequency of the fast oscillation which here corresponds to the zeroth mode increases slightly with amplitude, in contrast to all other modes (P_n, $n \geqslant 2$) which decrease with the square of the amplitude. The reason for this is that P_0 does not couple with any other mode through nonlinear terms.

8. Concluding remarks

The hybrid finite element–boundary element formulation developed here resulted in an accurate and efficient simulation of the shell oscillations with time. Significant nonlinear effects were captured, such as mode coupling, mode resonance and most importantly the centring mechanism has been explained definitively. For a given ratio of the inner to outer radii, there is an upper limit for the amplitude of the initial disturbance, beyond which either the two surfaces touch each other or the growth of higher modes appears.

Refinement of the spatial and temporal resolution was the only means of smoothing employed. This provided accurate results without introducing numerical damping or resorting to excessively large system matrices and prohibitive computation times. For more severe initial disturbances, high modes grow too fast for the time and space discretization to capture them. When the two surfaces tend to touch each other, refinement does not help since then the entire problem formulation must be changed in order to account for multivalued surfaces and new physical forces.

The results obtained indicate that, although nonlinear effects cause the oscillatory motion of the centres of mass around the concentric configuration, they do not suffice for the complete explanation of the experimental observations. To this end, viscous effects must be included in order to damp out the slow motion. This oscillatory motion becomes faster for larger distortions and for an intermediate value of the ratio of radii, indicating that it is indeed a nonlinear effect. As expected, the frequency of the individual modes decreases with the square of the amplitude. Both the bubble and the sloshing mode conform to the above observations. Compressibility of the gas in the bubble does not change the overall picture. It does give rise, however, to interesting resonance phenomena that may further accelerate the centring mechanism.

This research was supported by the Fluid Mechanics Program of the National Science Foundation under grant no. MSM-8705735 and the New York Science and Technology Foundation under grant no. SSF(88)-06. Usage of the Cornell National Supercomputer Facilities (CNSF) and the graphics software developed by Dr A. Poslinski are gratefully acknowledged. Discussions with Professor H. Segur are greatly appreciated.

REFERENCES

ABRAMOWITZ, M. & STEGUN, I. A. 1972 *Handbook of Mathematical Functions*. Dover.

BAKER, G. R., MEIRON, D. I. & ORSZAG, S. A. 1982 Generalized vortex methods for free-surface flow problems. *J. Fluid Mech.* **123**, 477–501.

BAKER, G. R., MEIRON, D. I. & ORSZAG, S. A. 1984 Boundary integral methods for axisymmetric and three-dimensional Rayleigh–Taylor instability problems. *Physica* **12D**, 19–31.

BAKER, G. R. & SHELLEY, M. J. 1986 Boundary integral techniques for multi-connected domains. *J. Comput. Phys.* **64**, 112–132.

BENJAMIN, T. B. 1989 Note on shape oscillations of bubbles. *J. Fluid Mech.* **203**, 419–424.

DE BOOR, C. 1978 *A Practical Guide to Splines*. Springer.

DOLD, J. W. & PEREGRINE, D. H. 1984 Steep unsteady water waves: an efficient computational scheme. In *Proc. 19th Intl Conf. on Coastal Engineering, Houston*, pp. 955–967.

DOMMERMUTH, D. G. & YUE, D. K. P. 1987 Numerical simulations of nonlinear axisymmetric flows with a free surface. *J. Fluid Mech.* **178**, 195–219.

HENDRICKS, C. D. 1982 Inertial confinement fusion targets. In *Proc. Second Intl Colloq. Drops and Bubbles* (ed. D. H. Le Croissette), pp. 88–93. Jet Propulsion Laboratory.

JOHNSON, R. E. & SADHAL, S. S. 1985 Fluid mechanics of compound multiphase drops and bubbles. *Ann. Rev. Fluid Mech.* **17**, 289–320.

KELLOGG, O. D. 1953 *Foundations of Potential Theory*. Dover.

KENDALL, J. M. 1986 Experiments on annular liquid jet instability and on the formation of liquid shells. *Phys. Fluids* **29**, 2086–2094.

KRASNY, R. 1986 A study of singularity formation in a vortex sheet by the point-vortex approximation. *J. Fluid Mech.* **167**, 65–93.

LACHAT, J. C. & WATSON, J. O. 1976 Effective numerical treatment of boundary integral equations: a formulation for three-dimensional elastostatics. *Intl J. Numer. Meth. Engng* **10**, 991–1005.

LAMB, H. 1932 *Hydrodynamics*, 6th edn. Cambridge University Press.

LANDMAN, K. A. 1985 Stability of a viscous compound fluid drop. *AIChE J.* **31**, 567–573.

LEE, C. P. & WANG, T. G. 1988 The centring dynamics of a thin liquid shell in capillary oscillations. *J. Fluid Mech.* **188**, 411–435.

LEE, M. C., FENG, I. A., ELLEMAN, D. D., WANG, T. G. & YOUNG, A. T. 1982 Generation of a strong core-centering force in a submillimeter compound droplet system. In *Proc. Second Intl Colloq. on Drops and Bubbles* (ed. D. H. Le Croissette), pp. 107–111. Jet Propulsion Laboratory.

LONGUET-HIGGINS, M. S. 1989*a* Monopole emission of sound by asymmetric bubble oscillations. Part 1. Normal modes. *J. Fluid Mech.* **201**, 525–541.

LONGUET-HIGGINS, M. S. 1989*b* Some integral theorems relating to the oscillations of bubbles. *J. Fluid Mech.* **204**, 159–166.

LONGUET-HIGGINS, M. S. & COKELET, E. D. 1976 The deformation of steep surface waves on water I. A numerical method of computation. *Proc. R. Soc. Lond.* A **350**, 1–26.

LUNDGREN, T. S. & MANSOUR, N. N. 1988 Oscillations of drops in zero gravity with weak viscous effects. *J. Fluid Mech.* **194**, 479–510.

MILES, J. W. 1977 On Hamilton's principle for surface waves. *J. Fluid Mech.* **83**, 153–158.

MOORE, D. W. 1981 On the point vortex method. *SIAM J. Sci. Statist. Comput.* **2**, 65–84.

MOORE, D. W. 1982 A point vortex method applied to interfacial waves. In *Vortex Motion* (ed. H. G. Hornung & E. A. Muller), pp. 97–105.

PATZER, J. F. & HOMSY, G. M. 1975 Hydrodynamic stability of thin spherically concentric fluid shells. *J. Colloid Interface Sci.* **51**, 499–508.

PELEKASIS, N. A. 1991 Ph.D. thesis, SUNY at Buffalo (in preparation).

PELEKASIS, N. A., TSAMOPOULOS, J. A. & MANOLIS, G. D. 1990 Equilibrium shapes and stability of charged and conducting drops. *Phys. Fluids* A **2**, 1328–1340.

PELEKASIS, N. A., TSAMOPOULOS, J. A. & MANOLIS, G. D. 1991 A hybrid finite-boundary element method for inviscid flows with free surface (submitted).

PULLIN, D. I. 1982 Numerical studies of surface-tension effects in nonlinear Kelvin–Helmholtz and Rayleigh–Taylor instability. *J. Fluid Mech.* **119**, 507–532.

ROSENHEAD, L. 1931 The formation of vortices from a surface of discontinuity. *Proc. R. Soc. Lond.* A **134**, 170–192.

SAFFREN, M., ELLEMAN, D. D. & RHIM, W. K. 1982 Normal modes of a compound drop. In *Proc. Second Intl Colloq. Drops and Bubbles* (ed. D. H. Le Croissette), pp. 7–14. Jet Propulsion Laboratory.

TADJBAKHSH, I. & KELLER, J. B. 1960 Standing surface waves of finite amplitude. *J. Fluid Mech.* **8**, 442–451.

TSAMOPOULOS, J. A. & BROWN, R. A. 1983 Nonlinear oscillations of inviscid drops and bubbles. *J. Fluid Mech.* **127**, 519–537.

TSAMOPOULOS, J. A. & BROWN, R. A. 1984 Resonant oscillations of inviscid charged drops. *J. Fluid Mech.* **147**, 373–395.

TSAMOPOULOS, J. A. & BROWN, R. A. 1987 Dynamic centering of liquid shells. *Phys. Fluids* **30**, 27–35.

ZAKHAROV, V. E. 1968 Stability of periodic waves of finite amplitude on the surface of a deep fluid. *J. Appl. Mech. Tech. Phys.* **2**, 190–194 [transl. of *Zh. Prikl. Mekh. Tekh. Fiz.* **9**(2), 86–94].